

High density molecular clumps around protostellar candidates

R. Cesaroni, M. Felli, and C.M. Walmsley

Osservatorio Astrofisico di Arcetri, Largo E. Fermi 5, I-50125 Firenze, Italy

Received November 20, 1998; accepted January 20, 1999

Abstract. There are several indications that strong H₂O maser emission arises at the very beginning of the evolution of a massive star and disappears when an HII region becomes detectable in the radio continuum. If this is the case, one expects to find dense hot molecular gas surrounding embedded far IR sources coincident with H₂O masers. In order to test this hypothesis, we have used the Pico Veleta 30-m radiotelescope to search for molecular line emission towards a sample of 12 H₂O masers located in regions of massive star formation, but *not* directly associated with bright compact radio HII regions, with the intention to identify the sites of newly born massive (proto)stars in their *earliest* stages and to study their properties.

Our main goals were: a) to confirm the hypothesis that the H₂O masers not associated with compact radio continuum emission are indeed located at the centre of high density clumps within a molecular cloud; b) to use several molecular transitions (namely: ¹³CO(2–1), CS(3–2), C³⁴S(2–1), C³⁴S(3–2), C³⁴S(5–4), HCN(1–0), CH₃CN(8–7), CH₃CN(12–11), HCO⁺(1–0), CH₃OH(3–2), CH₃OH(5–4)) in order to derive information on the size, kinematics, temperature, density, and ionisation degree of the molecular gas in the places where star formation has just begun, as well as to search for the presence of outflows on scale sizes of 10'' – 30''.

In this paper we present the large amount of data obtained at Pico Veleta in a compressed way, but still sufficiently ample to give usable informations for further studies. General results from a first analysis of the data are also presented.

Our first goal is amply verified since in all cases and in molecules tracing high density gas we find a barely resolved peak at the position of the maser, confirming the validity of our selection criteria. Our sample thus provides a valid reference list of regions of massive star formation in their earliest phases.

As far as the second goal is concerned, the large variety of intensity ratios of different molecules, as well as of other

derived parameters, point out that the molecular clumps where star formation is taking place are far from identical and that chemical evolution and influence of the newborn star may amply affect the line intensity ratios.

In some cases small scale (seconds of arc) outflows were detected, not necessarily related to the minute of arc scale outflows present in the same regions.

More detailed studies of each region are presented in separate papers.

Key words: ISM: clouds — ISM: molecules — radio lines: interstellar

1. Introduction

Over the last two decades, there have been great efforts to identify what might be called the “missing link” of astronomy: the protostar. Even the most optimistic agree that this work has given questionable results. The explanation may be either the brevity of the protostellar phase or the lack of an effective tool to sample the high density, optically thick, collapsing regions where stars form. Whatever the explanation, from an observational point of view, it is clear that the first step is to define the criteria which identify embedded young stars in their very earliest evolutionary stages.

The material surrounding such embedded young stars, presumably related to the dense condensation existing prior to star formation, is confined to a very small region, of the order of a few seconds of arc (0.1 pc typically), and its presence may be overshadowed by larger structures. The precise problem depends on the observing technique: (i) in the radio continuum by the extended HII regions generated by older generation massive stars; (ii) in molecular lines by larger scale low density (but optically thick) molecular clouds; and finally (iii) in the near and far IR by radiation of more luminous nearby stars in the same complex. Hence, high resolution and selective molecular

tracers are needed to distinguish the emission from the environment of the youngest stars from that emanating from the surrounding medium.

We believe that H_2O masers (of star forming type, to distinguish them from those associated with late type stars) represent an excellent tracer of the earliest stages of star formation. The advantage of using H_2O masers as tracers is twofold: firstly their positions are known with very high accuracy ($\sim 0.1''$) and hence one can limit the region to be studied to a small field around the masers. Secondly, several observations suggest that *H_2O masers are closely related to the earliest high density phases of the formation of massive stars, prior to the development of an ultracompact (UC) HII region* (Tofani et al. 1995 hereafter TFTH; Hofner & Churchwell 1996; Cesaroni et al. 1997a; Cesaroni et al. 1997b; Testi et al. 1998; Plume et al. 1992; Plume et al. 1997; Codella et al. 1997).

H_2O masers of star forming type have been found in the surroundings of HII regions (Wood & Churchwell 1989a; Churchwell et al. 1990). However, it is becoming more and more evident that they are not associated with the diffuse ionised gas of evolved HII regions, but with dense molecular clumps present in the same area, which in some cases contain embedded UC HII regions (e.g. Cesaroni et al. 1991). Recently, observations with high spatial resolution ($\ll 1''$) have shown that there are several cases where no UC HII region is associated with the H_2O masers (Hunter et al. 1994; TFTH). Considering that an H_2O maser requires a neighbouring stellar source in order to excite it (Elitzur et al. 1989), the lack of a compact radio continuum source suggests that the embedded massive star is not capable of exciting an observable UC HII region. This might be because the UC HII region is so optically thick and highly self-absorbed to be undetectable at radio wavelengths and thus very dense and very young.

The complex scenario that is emerging from more detailed studies of selected star forming regions suggests that different and probably independent episodes of star formation, each with its own HII region, may have occurred in the same complex and that H_2O masers are associated with the most recent episodes (Hunter et al. 1994; Felli et al. 1997; Schreyer et al. 1997).

At the same time, in several objects, the H_2O maser spots show an excellent positional agreement with molecular clumps revealed in several transitions and with far IR or sub-mm continuum peaks (i.e. dust), but not with radio continuum peaks. This situation is for instance seen in W3(OH) (Turner & Welch 1984; Wink et al. 1994; Wyrowski et al. 1997) where the molecular emission comes from the position of the H_2O maser, which is offset by $\sim 6''$ (0.06 pc) from a strong UC HII region. In Orion itself, the H_2O masers are *not* associated with the diffuse gas ionised by the Trapezium Cluster, but with the molecular peak in the BN/KL region and with a very weak unresolved radio source (component I: Churchwell et al. 1987; Felli et al. 1993; Gaume et al. 1998).

VLA observations in the (4, 4) inversion transition of ammonia towards other UC HII regions (Cesaroni et al. 1994) lead to similar conclusions: both H_2O masers and $\text{NH}_3(4, 4)$ emission arise from the same position, well apart from continuum peaks. Cesaroni et al. (1994) conclude that the $\text{H}_2\text{O} - \text{NH}_3$ clumps are likely to be the site of massive star formation. Methyl cyanide seems to trace the same high density clumps (Olimi et al. 1993, 1996, 1996b) and one concludes that these are examples of the “hot core” phenomenon, where the presence of a nearby luminous star causes the evaporation of dust grain ice mantles in the surrounding medium and consequently enhances the abundance of several molecular species (see Millar 1997 and Ohishi 1997).

With this in mind, we have selected a sample of 12 H_2O maser sources that radio continuum observations with high spatial resolution and sensitivity (TFTH) have shown to be well separated ($> 10''$) from the closest HII region. A few of these objects have already been observed in some molecular lines (see Krügel et al. 1987; Serabyn et al. 1993) and most of them have been detected in the CS(7 – 6) and CO(3 – 2) transitions (Plume et al. 1992, 1997). Our goal is that of obtaining a full picture with high single dish resolution ($10'' - 30''$) of the molecular environment of the water masers. For this purpose, we have used IRAM 30-m observations of the $\text{C}^{34}\text{S}(2 - 1)$, (3 – 2) and (5 – 4) transitions to estimate the size and density of the associated molecular clump (cf. Cesaroni et al. 1991). We have also observed the $\text{HCO}^+(1 - 0)$ and $\text{HCN}(1 - 0)$ lines with the aim of studying the dynamics and ionisation degree of the molecular gas. Note that the $\text{HCO}^+(1 - 0)$ line may be a good tracer for infall (see e.g. Welch et al. 1987 and Rudolph et al. 1993), as well as of outflow (Cesaroni et al. 1997b). Observations of the $\text{CH}_3\text{OH}(3 - 2)$ and (5 – 4) transitions and $\text{CH}_3\text{CN}(8 - 7)$ and (12 – 11) transitions were also carried out with the aim of detecting the “hot core” if present, as well as to determine the clump density and temperature. Methyl cyanide and methanol have advantages from this point of view as one can observe several transitions of differing excitation within one bandwidth. The relative intensities of these lines are thus essentially independent of calibration errors. Moreover, we have available LVG statistical equilibrium codes which permit us to interpret the results (see e.g. Bachiller et al. 1998; Walmsley 1987; Olmi et al. 1993) Finally, $^{13}\text{CO}(2 - 1)$ and CS(3 – 2) were also mapped, in order to obtain information on the larger scale molecular gas distribution.

Our survey does indeed show that *all* our targets are associated with molecular clumps centred on the H_2O maser spots. In this respect, our results are analogous to those of Plume et al. (1992, 1997), who searched for high density molecular tracers in several transitions of CS and C^{34}S towards a large number of H_2O masers. The essential difference is that we have carried out a more detailed mapping of a restricted number of objects, whereas Plume et al. merely observed towards the water maser position.

Table 1. Coordinates of the field centres and fluxes of the associated IRAS sources

Name	H ₂ O ^a	α^b (1950)	δ^b (1950)	IRAS #	12 ^c	25 ^c	60 ^c	100 ^c	25/12	60/12
NGC 281-W	C3	00:49:28.8	56:17:33	00494+5617	<1.80	13.4	330	1 170	0.869	2.261
AFGL5142	C4	05:27:30.0	33:45:40	05274+3345	6.89	69.4	449	905	1.003	1.814
S233	C1	05:35:51.2	35:44:13	05358+3543	5.61	74.6	722	1 309	1.124	2.110
GGD 4	C2	05:37:21.1	23:49:22	05373+2349	9.03	26.5	125	192	0.468	1.141
S235 B	C1	05:37:31.9	35:40:18	05375+3540	28.20	226.0	1 710	1 640	0.904	1.783
MON R2	C1	06:05:21.6	-06:22:28	06053-0622	470.00	4 100.0	13 100	20 200	0.941	1.445
GGD 12-15	C1	06:08:25.7	-06:10:50	06084-0611	27.20	602.0	3 610	4 840	1.345	2.123
NGC 2264-C	C1	06:38:25.4	09:32:14	06384+0932	146.00	325.0	911	1 560	0.348	0.795
IRAS 20126+4104	C3	20:12:41.0	41:04:21	20126+4104	<2.53	108.9	1 381	1 947	1.634	2.737
IC 1396-N	C1	21:39:09.8	58:02:31	21391+5802	0.82	9.8	146	410	1.079	2.252
L1204-G	C2	22:19:49.8	63:36:29	22198+6336	<0.27	25.6	189	400	1.982	2.850
IRAS 23151+5912	C1	23:15:08.4	59:12:23	23151+5912	50.90	203.0	1 110	1 010	0.601	1.339

^a Maser component with higher peak flux from TFTH.

^b Coordinates of the maser peak from TFTH rounded to 1".

^c Fluxes in Jy in the four IRAS bands (12, 25, 60 and 100 μ m).

Some of the results presented here have been covered in earlier publications but, for completeness, here we present the whole sample observed with the 30-m here. Partial results for S235 A–B were reported in Felli et al. (1997). A detailed analysis of the survey observations for IRAS 20126+4104 as well as comparison with Plateau de Bure interferometric observations and near IR observations were presented by Cesaroni et al. (1997a). These two objects are fairly typical of the complete sample.

In Sect. 2 of this article, we summarise the properties of the sample and give the water maser coordinates from TFTH. In Sect. 3, we explain the procedures used during the observations and data reduction. In Sect. 4, we present the data giving both line parameters towards the central positions and maps. We also discuss the properties of individual sources in Sect. 5. Finally, in Sect. 6, we summarise our conclusions.

2. Properties of the input sample

We shall briefly summarise in this section the main properties which characterise the sources in our sample.

First, a word on the nomenclature (see e.g. Table 1) is useful. We have adopted that used by TFTH, but this should be treated only as indicative because several other names are often in use and also because these names may refer to objects much more extended than those studied by us. To avoid confusion, it is best to consult the coordinates given in Table 1. These refer to the strongest H₂O maser component found in the VLA observations of TFTH. NGC 2264 has been renamed NGC 2264-C to avoid confusion with other molecular outflows present in the same molecular cloud which bear similar names (it is component C in the original outflow survey of the

Monoceros OB1 molecular cloud made by Margulis et al. 1988). Schreyer et al. (1997) call this source NGC 2264 IRS1.

The basic common property of the sources in our sample is that in all the fields, there is an H₂O maser (Comoretto et al. 1990; Brand et al. 1993) of star forming type (Palagi et al. 1993). All the H₂O masers were observed with the VLA and have positions with 0.1" accuracy (TFTH). They were also observed with the VLA in the continuum at 8.4 GHz and no small diameter source (size $\leq 1''$) with flux density greater than 0.3 mJy (3σ) was found within a radius of $\sim 10''$ of the maser position (TFTH). The only exception is AFGL5142, where a 0.85 mJy (at 8.4 GHz) source is present at the position of the two brightest maser components. It was included because multiwavelength observations had already been obtained, showing a complex outflow morphology (Hunter et al. 1995).

In all fields, there is an IRAS source close to the H₂O maser (within $\sim 30''$). The IRAS name, the four IRAS fluxes and the 25/12 and 60/12 colours¹ are given in Table 1. All but two (GGD 4 and NGC 2264-C) fall in the box of the 25/12 – 60/12 colour–colour plot that Wood & Churchwell (1989b) define as that occupied by UC HII regions ($25/12 \geq 0.57$, $60/12 \geq 1.3$). However, they are clearly not UC HII regions as normally defined in that their radio continuum luminosity is extremely small. One should also note that a direct physical relationship between the IRAS source and the H₂O maser (more specifically, with the young star that powers the maser) is far from being firmly established. This is partly because the accuracy of the IRAS position is at least two orders of magnitude worse than that of the H₂O masers. Secondly,

¹ $i/j = \text{Log}[F_i/F_j]$.

Table 2. Velocities of the large scale CO molecular outflows (see TFTH and references therein)

Name	V_P	$V_{\text{blue}}^{\text{max}}$	$V_{\text{blue}}^{\text{min}}$	$V_{\text{red}}^{\text{min}}$	$V_{\text{red}}^{\text{max}}$
NGC 281-W	-30.5	-40.0	-34.0	-28.0	-20.0
AFGL5142	-3.5	-18.0	-8.0	2.0	12.0
S233	-17.2	-30.0	-21.0	-12.0	-6.0
GGD 4	3.0	-15.0	-3.0	7.0	16.0
S235 B	-17.0	-24.0	-20.0	-13.0	-6.0
MONR2	11.0	-2.0	6.0	14.0	22.0
GGD 12-15	12.0	-6.0	8.0	14.0	30.0
NGC 2264-C	8.0	-8.0	4.0	12.0	24.0
IRAS 20126+4104	-3.7	-25.8	-7.9	-0.1	37.3
IC 1396-N	0.7	-21.5	-7.8	7.8	21.4
L1204-G	-10.8	-25.0	-15.0	-5.0	5.0
IRAS 23151+5912	-54.0	-70.0	-58.0	-52.5	-44.0

the IRAS source is in most cases associated with a cluster of newly formed stars. The large IRAS beam collects the emission from the entire star forming complex (Hunter et al. 1994; Testi et al. 1994; Hunter et al. 1995; Felli et al. 1997) and the separation of the contribution of different stars is impossible. In other words, the presence of an IRAS source confirms that we are indeed looking at star forming regions, but the IRAS fluxes cannot be unambiguously attributed to the young stellar object (YSO) associated with the H₂O masers.

The sources of our sample are located in known molecular clouds and are associated with large scale CO molecular outflows (see Fukui et al. 1993 for the references). However, we do not aim in this work to better define the large scale outflows (which are not necessarily related to the YSO associated with the water masers) because this would require larger scale maps than we were able to carry out. Similarly, we have not attempted to provide large scale maps of the “ambient” molecular cloud. Our aim has rather been to search for the presence of high density clumps in a small region around the maser positions using high density tracers. In Table 2, we give for further reference the peak velocity of the CO cloud (V_P) and the two velocities that define the inner (min) and outer (max) ranges of the blue and red large scale outflows.

In Table 3 we give a list of parameters derived from the literature using the distance (d) adopted by TFTH: the IRAS (bolometric) luminosity (L_{FIR}), the H₂O maser luminosity ($L_{\text{H}_2\text{O}}$), the mechanical luminosity of the large scale CO outflow (L_{CO}), the expected flux of Lyman continuum photons (N_L^{exp}) assuming a single ionising star with luminosity equal to the IRAS luminosity, and the expected radio flux density at 8.4 GHz (S_{exp}) from an optically thin HII region. One sees from the range of L_{FIR} ($200 - 3 \cdot 10^4 L_{\odot}$) that our sample is not restricted to proto O-B stars but also contains embedded stars of later spectral type. Indeed in these latter cases (GGD 4, IC 1396-N, L1204-G), it is not surprising that no radio continuum emission was observed by TFTH because S_{exp} was

below the detection limits (see Table 3). Nevertheless, we thought it interesting to include them in this survey in order to see if they share the molecular morphology of the high luminosity objects.

Finally, it is important to be aware that all of these star forming regions have been imaged in the near IR (Hodapp 1994; Testi et al. 1999). In almost all cases, a cluster of K' -band sources was found (Hodapp 1994), clearly revealing the complex nature of the star forming region and showing that high resolution observations are needed to distinguish different stars in the same cluster.

3. Observations and data reduction

The observations were carried out in July 1994 using the IRAM 30-m radiotelescope at Pico Veleta (Spain). Spectra were obtained in position switching with a reference position at 30' offset or using the wobbler (i.e. a nutating secondary) with a beam-throw of 240'' and a phase duration of 2 s. The calibration was performed with the chopper wheel method with both hot (sky and absorber) and cold (nitrogen) loads. The calibration was verified on well-known molecular sources and by continuum scans across Jupiter, Uranus, Mars, and Saturn: we found it to be accurate to within 20% at all frequencies. The absolute pointing was good to 4''. The conversion factor from main beam brightness temperature (T_{MB}) to flux density is 4.7 Jy K⁻¹. The backends were: 1) two filterbanks spanning 512 MHz and providing a frequency resolution of 1 MHz; 2) a filterbank with 25.6 MHz bandwidth and 100 kHz resolution; and 3) an autocorrelator used in various high spectral resolution configurations, so that three bands could be observed simultaneously.

Two 3 × 3 point raster maps centred on the H₂O maser position (see Table 1) were made; one with 24'' sampling, the other with 12''. In some cases, larger fields were covered to complete the mapping of the cloud. The integration time (ON + OFF) per point was 1 min and the maps were repeated up to three times and then averaged. The pointing and the focus were verified regularly (every hour) on nearby continuum sources. A total of 7 molecular species and 11 rotational transitions were mapped. They are summarised in Table 4 together with the corresponding half power beam width (HPBW) of the telescope.

The data were reduced with the CLASS and GRAPHIC programs of the Grenoble Astrophysical Group (GAG) package. A polynomial baseline was removed from each spectrum and then spectra taken towards the same position were averaged; however, in cases where more than one map had been taken in the same tracer towards a given source, the different maps were compared before average, to ensure consistency between them. Finally, channel maps and integrated maps in suitable velocity intervals were created.

Table 3. Derived source parameters

Name	d (kpc)	$\text{Log}L_{\text{FIR}}$ (L_{\odot})	$\text{Log}L_{\text{H}_2\text{O}}$ (L_{\odot})	$\text{Log}L_{\text{CO}}$ (L_{\odot})	$\text{Log}N_{\text{L}}^{\text{exp}}$	S_{exp} (mJy)
NGC 281-W	2.1	3.61	-4.60	0.18	45.0	2.4
AFGL5142	1.8	3.56	-4.42	-0.40	44.9	2.6
S233	1.8	3.71	-4.66		45.2	5.2
GGD 4	1.0	2.55	-5.82	2.30	42.5	$3.4 \cdot 10^{-2}$
S235 B	1.8	4.03	-5.44	-0.55	46.2	52.4
MON R2	0.8	4.39	-5.39	2.38	47.3	$3.3 \cdot 10^3$
GGD 12-15	1.0	3.90	-6.00	-3.77	45.8	67.6
NGC 2264-C	0.8	3.32	-6.43		44.4	4.6
IRAS 20126+4104	1.7	3.88	-5.09		45.8	23.4
IC 1396-N	0.7	2.32	-5.51	-1.70	42.1	$2.4 \cdot 10^{-2}$
L1204-G	0.9	2.56	-5.82		42.6	$5.3 \cdot 10^{-2}$
IRAS 23151+5912	3.5	4.49	-4.89	-0.03	47.6	$3.5 \cdot 10^2$

Table 4. Frequencies of observed molecular transitions and telescope HPBW

Line	ν (MHz)	HPBW (arcsec)
HCN(1-0)	88631.602	27
HCO ⁺ (1-0)	89188.516	27
C ³⁴ S(2-1)	96412.984	25
C ³⁴ S(3-2)	144617.141	17
CH ₃ OH(3-2)	145093.750 ^a	17
CS(3-2)	146969.049	17
CH ₃ CN(8-7)	147174.594 ^b	16
¹³ CO(2-1)	220398.686	11
CH ₃ CN(12-11)	220747.266 ^b	11
C ³⁴ S(5-4)	241016.172	10
CH ₃ OH(5-4)	241700.219 ^c	10

^a Frequency of the $3_0 - 2_0$ E transition.

^b Frequency of the $K = 0$ transition.

^c Frequency of the $5_0 - 4_0$ E1 transition.

4. Presentation of the data

Table 5 gives a summary of the results obtained, indicating which lines were observed and detected towards each source.

The amount of data that we have obtained is very large, considering that for each source and for each transition a data cube (α , δ , velocity) can be created. It is also difficult to express our results in the form of tables of line parameters. Some lines have very large signal-to-noise ratio (S/N) and allow detailed studies of line profiles, namely absorption dips and asymmetries in the core of the line and wings at large velocities (outflows). In other cases, the S/N is so low that we have a marginal detection only at the central position and very little information on the

line profile. We stress that in all tracers with sufficiently good S/N, the emission peaks at the position of the water masers (within the uncertainty related to the angular resolution and sampling of our maps). Thus, it seems highly probable that the gas clumps mapped by us are associated with the water maser as well as with the YSO.

While the individual spectra in our maps are available upon request², we have decided to present here the following information:

1. Spectra of all the transitions observed towards the peak position of our maps (namely the position of the H₂O maser). These figures show the velocity structure of the lines and the relative intensities of the transitions.
2. Contour plots of the velocity integrated intensity for each transition where we have sufficient S/N to allow mapping.
3. Tables with line parameters and other quantities of interest derived from the maps.
4. Contour plots in selected velocity ranges for the transitions with good S/N. These are shown only when asymmetries in the spatial distribution of the low or high velocity emission are present.

4.1. Spectra of molecular transitions

In Fig. 1 we plot the spectra of the ¹³CO, HCO⁺, CS, C³⁴S, and HCN lines observed towards all the sources. When one or several spectra are missing, this means that the corresponding lines were either not observed or not detected. We present in Fig. 2 the spectra of the CH₃CN and CH₃OH transitions.

We note that the strongest lines observed by us such as ¹³CO, HCN, HCO⁺, and – to some extent – CS show

² Contact R. Cesaroni.

Table 5. Summary of observed lines

Source	HCO ⁺ (1-0)	CS(3-2)	C ³⁴ S			HCN(1-0)	CH ₃ OH		¹³ CO(2-1)	CH ₃ CN	
			(2-1)	(3-2)	(5-4)		(3-2)	(5-4)		(8-7)	(12-11)
NGC 281-W	Y	Y	Y	Y	Y	Y	Y	Y	Y	Y	Y
AFGL5142	Y	Y	Y	Y	Y	Y	—	—	Y	Y	Y
S233	Y	Y	Y	Y	Y	Y	—	—	Y	Y	Y
GGD 4	—	—	N	Y	N	Y	—	—	Y	Y	N
S235 B	—	—	Y	Y	Y	Y	—	—	Y	Y	N
MONR2	—	—	Y	Y	Y	Y	—	—	Y	Y	N
GGD 12-15	—	—	Y	Y	N	Y	—	—	Y	N	N
NGC 2264-C	—	—	Y	Y	N	Y	—	—	Y	Y	N
20126+4104	Y	Y	Y	Y	Y	Y	Y	Y	Y	Y	Y
IC 1396-N	Y	Y	Y	Y	N	Y	Y	Y	Y	Y	N
L1204-G	Y	Y	Y	Y	N	Y	Y	Y	Y	Y	N
23151+5912	Y	Y	Y	Y	N	Y	—	—	Y	N	N

Note: Y = detected; N = non detected; — = non observed.

complex line profiles with wings suggestive of “outflow activity” (see for example Fig. 1 for NGC 281-W). In the case of less abundant species (e.g. C³⁴S), this is usually not the case but this may just be a question of sensitivity. It is interesting however that in some sources, the velocity of the C³⁴S(3-2) line (obtained with a Gaussian fit) corresponds to a dip in the profile of CS(3-2) (see e.g. IC 1396-N) suggesting high optical depth. In general, as discussed below, there is reason to believe that the “strong lines” are thick but one should note also that there are cases (e.g. S233) where the C³⁴S peak coincides with a peak in CS(3-2) suggesting the presence of distinct spatial and velocity components in the molecular cloud. A more detailed investigation of such line profiles and of their origin will be given in Sect. 5.

4.2. Integrated velocity contour plots

The simplest description of the emitting region in a given transition is obtained from the integrated emission in the line of interest. In Figs. 3 to 8 we show maps for all cases where the line emission was strong enough to be detected away from the central position. In particular, Figs. 3 and 4 refer to the “strong line” tracers, namely ¹³CO, HCN, HCO⁺, and CS, whereas Figs. 5 to 7 illustrate the distribution of the “weak line” tracers i.e. C³⁴S, CH₃CN, and CH₃OH. One sees that the latter transitions arise from regions smaller than those traced by the “strong lines”. Moreover, in all sources the C³⁴S emission coincides with the H₂O maser spots: although this is true for all lines, the C³⁴S emission is particularly significant since it is most probably optically thin whereas at least the “strong lines” are likely to be somewhat optically thick (see discussion in Sect. 4.5). Thus C³⁴S can be expected in crude fashion to be “representative” of the mass distribution in the dense molecular gas. We consider this to be strong evidence that we have identified the clump from which the young stars in the cluster surrounding the water masers have formed.

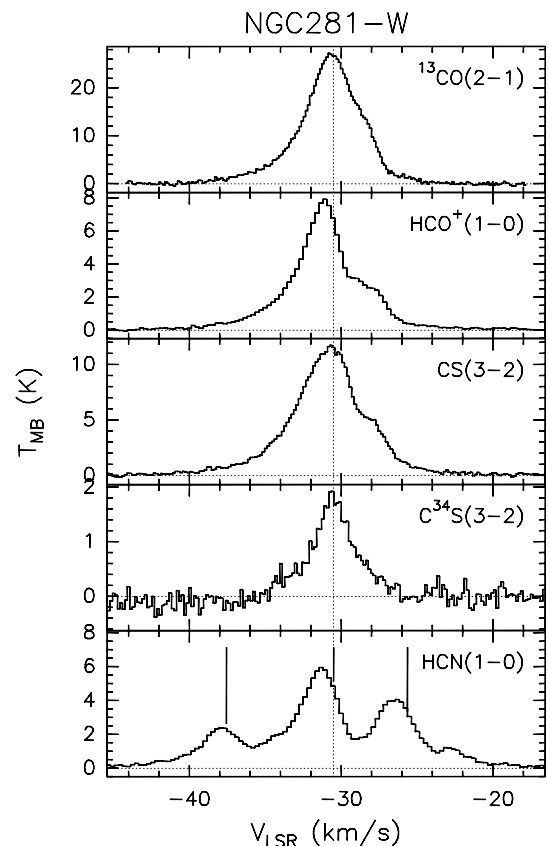


Fig. 1. a) Spectra of some rotational transitions observed towards the H₂O maser position (i.e. the map centre, see Table 1) in NGC 281-W. The main beam brightness temperature (T_{MB}) is plotted against the local standard of rest (LSR) velocity. The conversion factor from T_{MB} to flux density is 4.7 Jy K^{-1} . The dotted horizontal and vertical lines correspond respectively to $T_{\text{MB}} = 0 \text{ K}$ and to the V_{LSR} of the C³⁴S(3-2) line obtained with a Gaussian fit. The vertical lines in the bottom panel indicate the $F = 0-1$ (left), $2-1$ (centre), and $1-1$ (right) hyperfine components of the HCN(1-0) transition

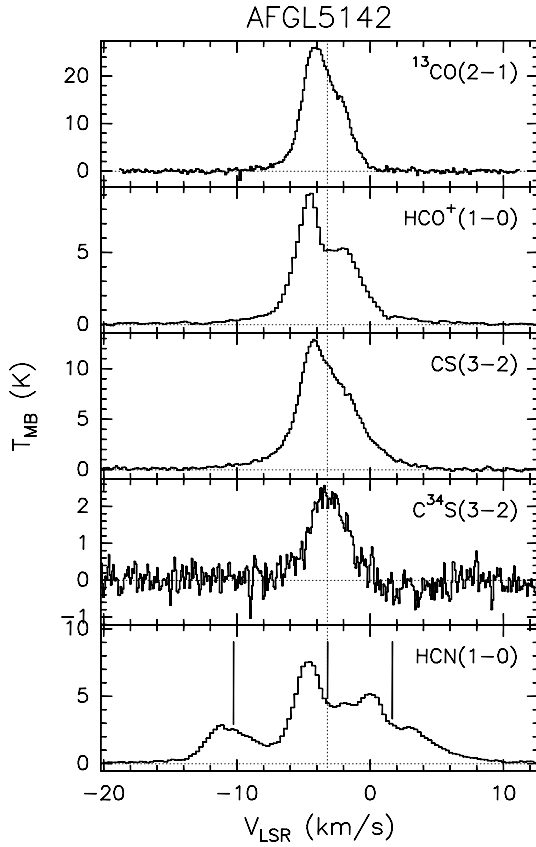


Fig. 1. b) Same as previous figure, for AFGL5142

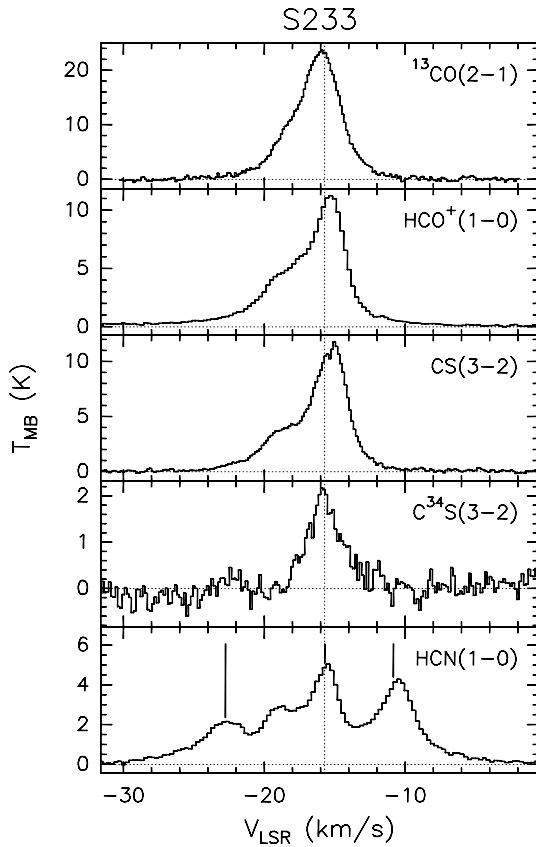


Fig. 1. c) Same as previous figure, for S233

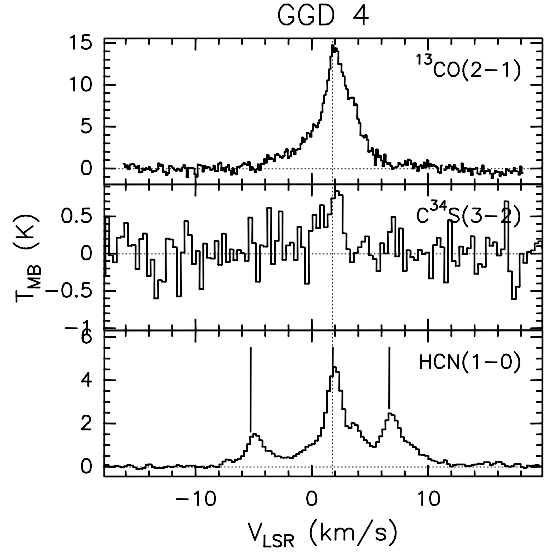


Fig. 1. d) Same as previous figure, for GGD 4

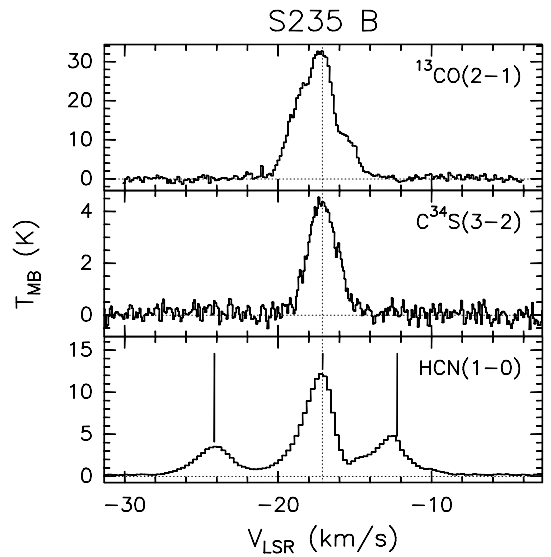


Fig. 1. e) Same as previous figure, for S235 B

4.3. Tables of relevant quantities

The line parameters at the peak position in the maps (corresponding to the maser position) are given in Tables 7 to 10. We have separated transitions with “simple” line profiles (such as e.g. ^{13}CO) from those where we have detected many components (such as CH_3OH) and hence give their parameters in different tables.

In Table 7, we list the measured line parameters for ^{13}CO , HCO^+ , CS , C^{34}S , and HCN . We give in column: 1) the source name; 2) the two extreme velocities (V_{min} and V_{max}) at which the line intensity becomes less than twice the RMS noise: thus $V_{\text{min}} - V_{\text{max}}$ is the full width at zero intensity (FWZI); 3) the peak temperature T_{peak} ; 4) the velocity of the peak V_{LSR} ; 5) the integral of the area under the profile; 6) the 1σ RMS of the spectrum. We note that, in the case of HCN , V_{min} and V_{max} are strongly

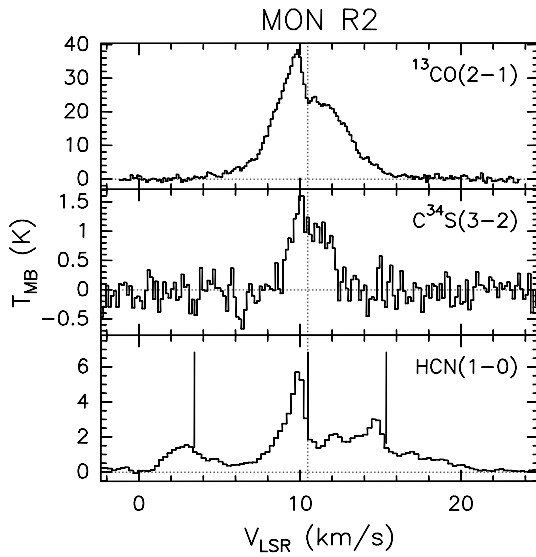


Fig. 1. f) Same as previous figure, for MON R2

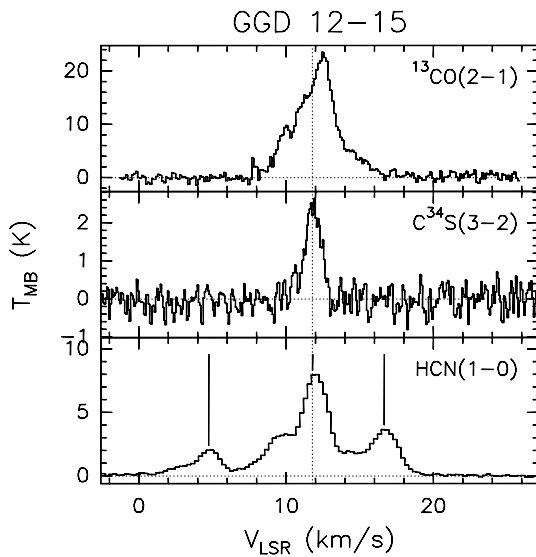


Fig. 1. g) Same as previous figure, for GGD 12-15

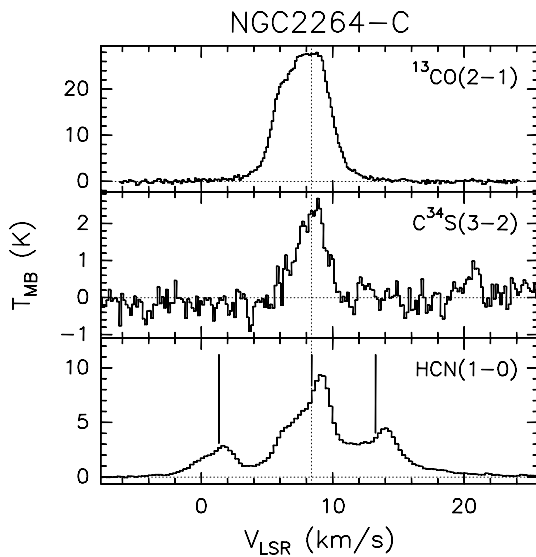


Fig. 1. h) Same as previous figure, for NGC 2264-C

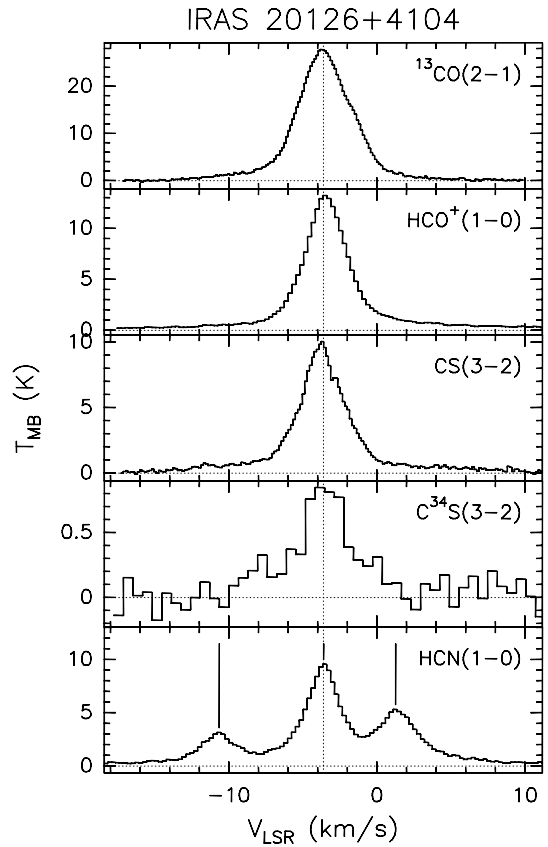


Fig. 1. i) Same as previous figure, for IRAS 20126+4104

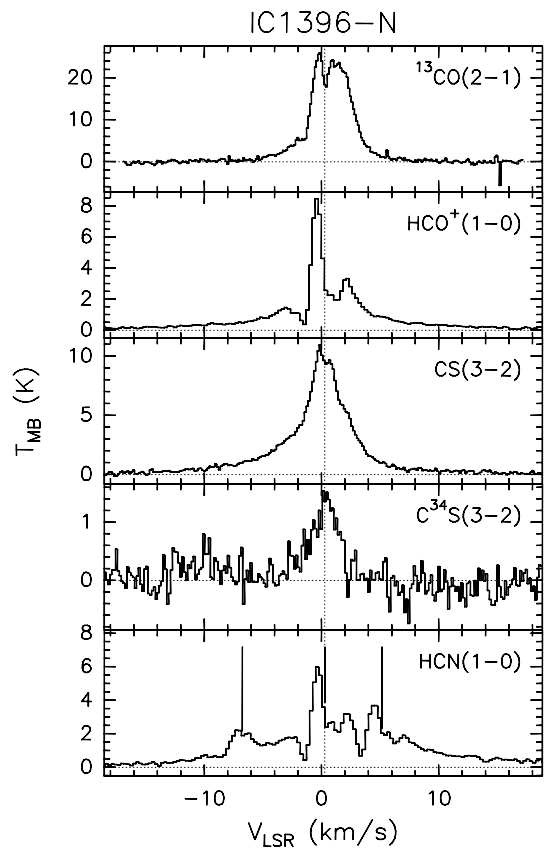


Fig. 1. j) Same as previous figure, for IC 1396-N

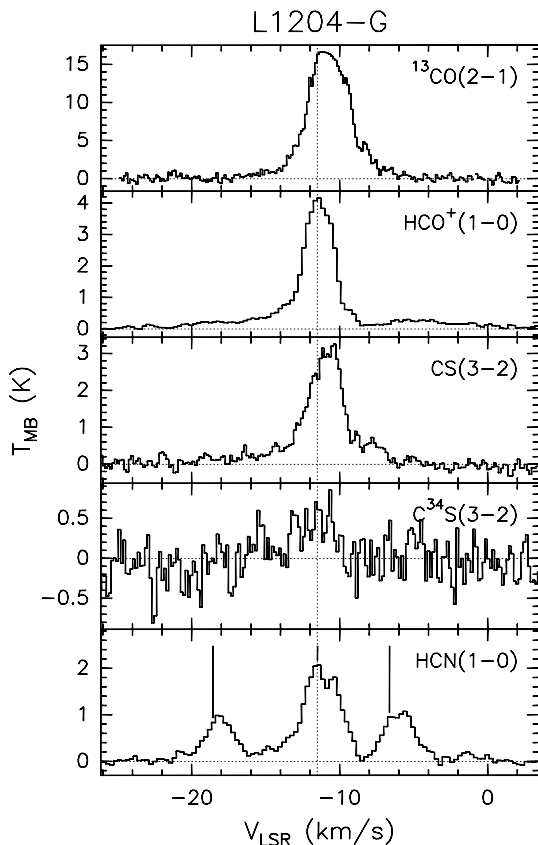


Fig. 1. k) Same as previous figure, for L1204-G

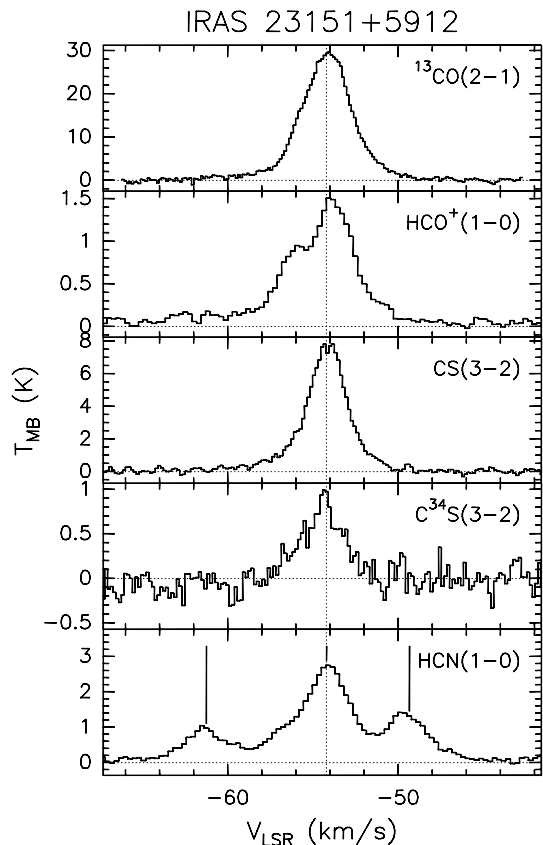


Fig. 1. l) Same as previous figure, for IRAS 23151+5912

affected by the $F = 0 - 1$ and $1 - 1$ hyperfine satellites which clearly widen the velocity range over which emission is detected.

There are a number of indications of high optical depth in the transitions observed by us. In the case of CS for example, we have observed both CS(3-2) and C³⁴S(3-2) in seven of the sources of our sample. From Table 7, one finds (excepting L1204-G where C³⁴S is very weak) that the ratio of CS(3-2)/C³⁴S(3-2) integrated intensities varies between 14.3 (IC 1396) and 8.5 (S233) whereas the corresponding ratio of peak intensities varies between 12.9 (AFGL5142) and 7.8 (23151+5912). These ratios should be compared with the local ISM value for ³²S/³⁴S of 22 (Wilson & Rood 1994). We conclude that the difference is due to moderate optical depth in CS(3-2). We also think it probable that HCN(1-0) is optically thick in many cases. Although the hyperfine satellites are usually blended with one another, from Table 8 it is clear that the intensity ratios vary substantially from the 5:3:1 (2-1:1-1-1:0-1) ratio expected in optically thin LTE.

Tables 9 and 10 list the parameters of the CH₃OH and CH₃CN transitions. These have been obtained by Gaussian fits, fixing the separation in frequency of different K -components to the laboratory values and forcing their line widths to be identical. We give the V_{LSR} and full width at half maximum ($FWHM$), and for each line the

integrated intensity. Note that Table 10 contains only the rotational transitions for which at least one K component was detected.

In Table 11 we give the measured full width at half power (FWHP) of the maps and the angular diameter after deconvolution (Θ_S) for a Gaussian source. The FWHP has been obtained as the diameter of a circle with the same area as that inside the 50% contour in the corresponding map. From this table, one sees that ¹³CO typically traces a component which extends beyond the borders of our map and thus the observed emission emanates only in part from the dense core associated with the water masers. HCN and HCO⁺ appear to trace extended material surrounding the core whereas the C³⁴S and CH₃OH transitions arise from gas relatively close to the water maser. It is plausible that the optically thick lines have more extended emission than optically thin transition and this may explain for example the slightly higher angular sizes seen in HCN, HCO⁺, and CS than in C³⁴S. In the case of methanol, there is evidence in the literature that it has high abundances in high temperature regions (Menten et al. 1986) and this may also influence the observed distribution.

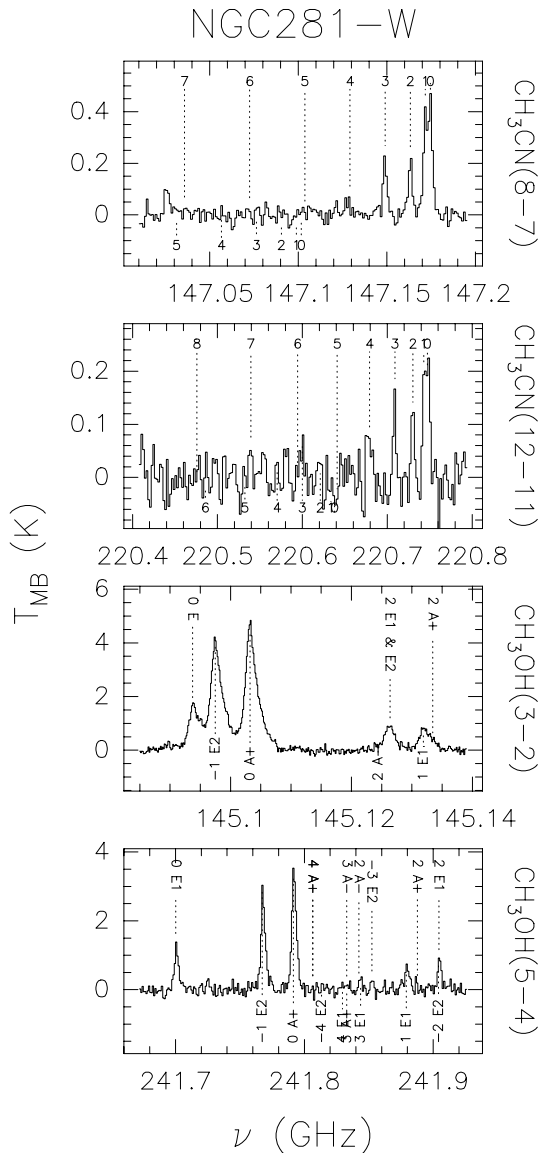


Fig. 2. a) Spectra of the CH_3CN and CH_3OH rotational transitions towards the H_2O maser position (i.e. the map centre, see Table 1) in NGC 281-W. The main beam brightness temperature (T_{MB}) is plotted against the frequency. The conversion factor from T_{MB} to flux density is 4.7 Jy K^{-1} . The dotted lines indicate the CH_3CN (lines above the spectrum) and $\text{CH}_3^{13}\text{CN}$ (from below), and the CH_3OH transitions; the corresponding quantum numbers are also shown

4.4. Line widths and line asymmetries

Because of its low abundance and relatively high critical density, C^{34}S is known to trace dense regions. Such regions are probably well defined, compact clumps characterised by a “simple” velocity field, as suggested by two facts: the $\text{C}^{34}\text{S}(3-2)$ profiles observed by us can be fitted with a single Gaussian component with $\text{FWHM} \sim 1/2$ as that of the $^{13}\text{CO}(1-0)$ line; and the angular diameter in the $\text{C}^{34}\text{S}(3-2)$ line is always $\lesssim 2$ times smaller than that in $^{13}\text{CO}(2-1)$ (see Table 7). Consequently, the peak velocity

of the $\text{C}^{34}\text{S}(3-2)$ can be assumed to represent the bulk velocity of the high density gas.

All these aspects suggest that the dynamics of the lower density gas (traced by ^{13}CO) is decoupled from that of the embedded high density clump (seen in C^{34}S). The greater linewidths and blue/red distribution of the low density gas originate from larger scale turbulence or motions of different sub-clumps and do not seem to be directly related to the presence of a high density clump.

We postpone to Sect. 5 a more detailed analysis of the molecular gas in each source, which requires a study of the cloud structure in different velocity intervals.

With this in mind, in Fig. 9 we have reproduced the $^{13}\text{CO}(2-1)$ profiles, aligning them to the $\text{C}^{34}\text{S}(3-2)$ peak velocity. In this way one can check for possible $^{13}\text{CO}(2-1)$ line asymmetries and differences between the ^{13}CO and C^{34}S peak velocities. For example, a dip in the ^{13}CO profile in correspondence of the C^{34}S peak may indicate self absorption due to temperature gradients in the molecular gas. Indeed, this occurs in two cases (MONR2 and IC 1396-N), although it might be due to absorption of foreground cooler gas at the same bulk velocity. The profile of the $^{13}\text{CO}(2-1)$ gas on the blue and red side of the $\text{C}^{34}\text{S}(3-2)$ peak does not show any systematic trend. In four sources the blue and red sides have almost equal intensity, in the remaining eight cases, four have larger integrated values on the blue side and four on the red side (with ratios of blue to red and vice-versa up to a factor two in both cases).

4.5. Line ratios in C^{34}S

On the basis of our C^{34}S measurements, we can attempt to constrain the density and temperature in the core surrounding the water masers. In Fig. 10, we show our measured $T_{\text{B}}(3-2)/T_{\text{B}}(2-1)$ and $T_{\text{B}}(5-4)/T_{\text{B}}(3-2)$ line brightness temperature ratios for C^{34}S in our sources; note that T_{B} has been obtained from Table 7, after correction for beam dilution using the sizes from Table 11 or (where not possible) with an assumed size of $20''$. We compare these with the results of Cesaroni et al. (1991), who mapped a sample of UC HII regions in the same transitions. It appears that the latter sample has slightly higher values of $T_{\text{B}}(5-4)/T_{\text{B}}(3-2)$ than our sources, but the difference is not large. Cesaroni et al. (1991) derived densities of order 10^6 cm^{-3} for their sample and we conclude that the sources in our sample have densities which are not greatly smaller.

We also show in Fig. 10 the results of LVG calculations for C^{34}S carried out assuming an abundance ratio $[\text{C}^{34}\text{S}]/[\text{H}_2]$ of 10^{-10} and temperatures of 50 K and 100 K. The abundance chosen is similar to that found for C^{34}S in other sources and has the effect that C^{34}S is optically thin for the parameter range considered by us. Thus, “trapping” is not of great importance. We have used the rate

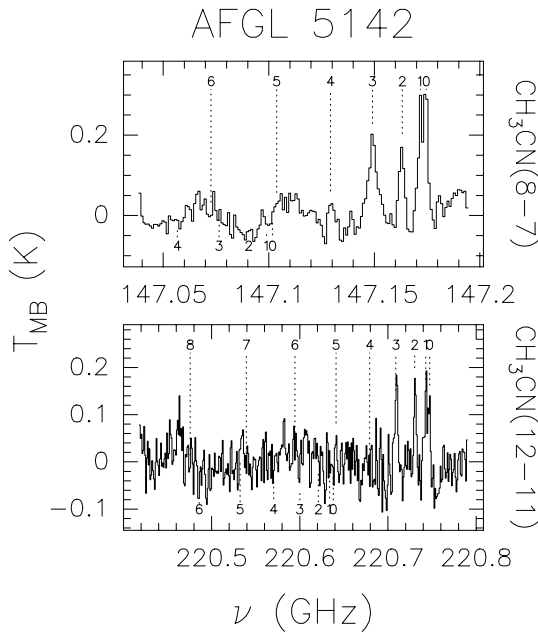


Fig. 2. b) Same as previous figure, for AFGL5142

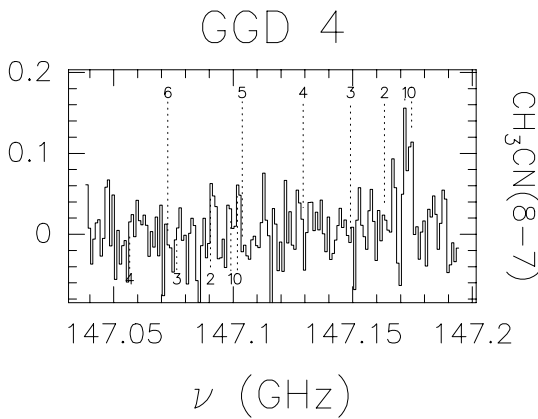


Fig. 2. c) Same as previous figure, for GGD 4

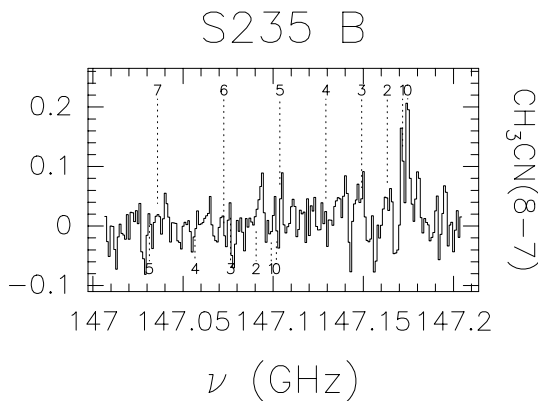


Fig. 2. d) Same as previous figure, for S235 B

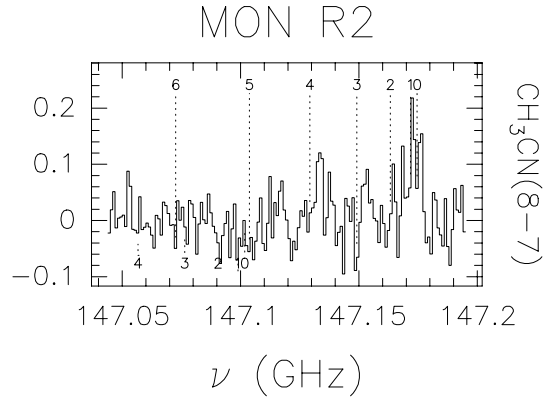


Fig. 2. e) Same as previous figure, for MON R2

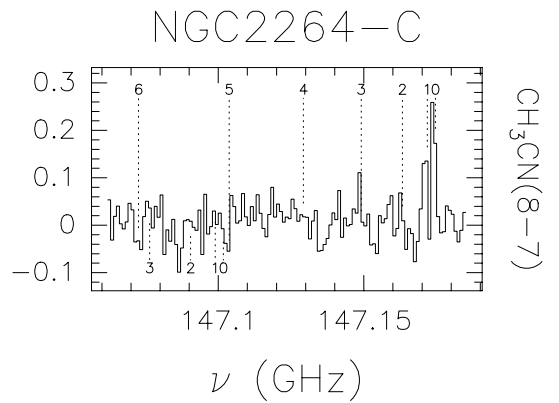


Fig. 2. f) Same as previous figure, for NGC 2264-C

coefficients discussed by Turner et al. (1992) but note that these are essentially the same as the earlier rates used by Cesaroni et al. (1991).

From Fig. 10 one sees that while the Cesaroni et al. (1991cwk) sample is in good agreement with model predictions, our sources tend to have $T_B(3-2)/T_B(2-1)$ intensity ratios close to or even larger than the maximum value allowed in LTE (2.25). This suggests that the temperature is high (above 30 K) and that probably there is a contribution to the (3-2) intensity from an unresolved hot compact source. The $T_B(5-4)/T_B(3-2)$ ratios suggest moreover that H_2 densities are approximately $5 \cdot 10^5 \text{ cm}^{-3}$: such a value is probably somewhat lower than found in the Cesaroni et al. (1991) study although the difference is small.

4.6. Boltzmann plots

The large number of methanol transitions detected in NGC 281-W, IRAS 20126+4104, IC 1396-N, and L1204-G make possible to derive temperature and column density estimates by means of the rotational diagram

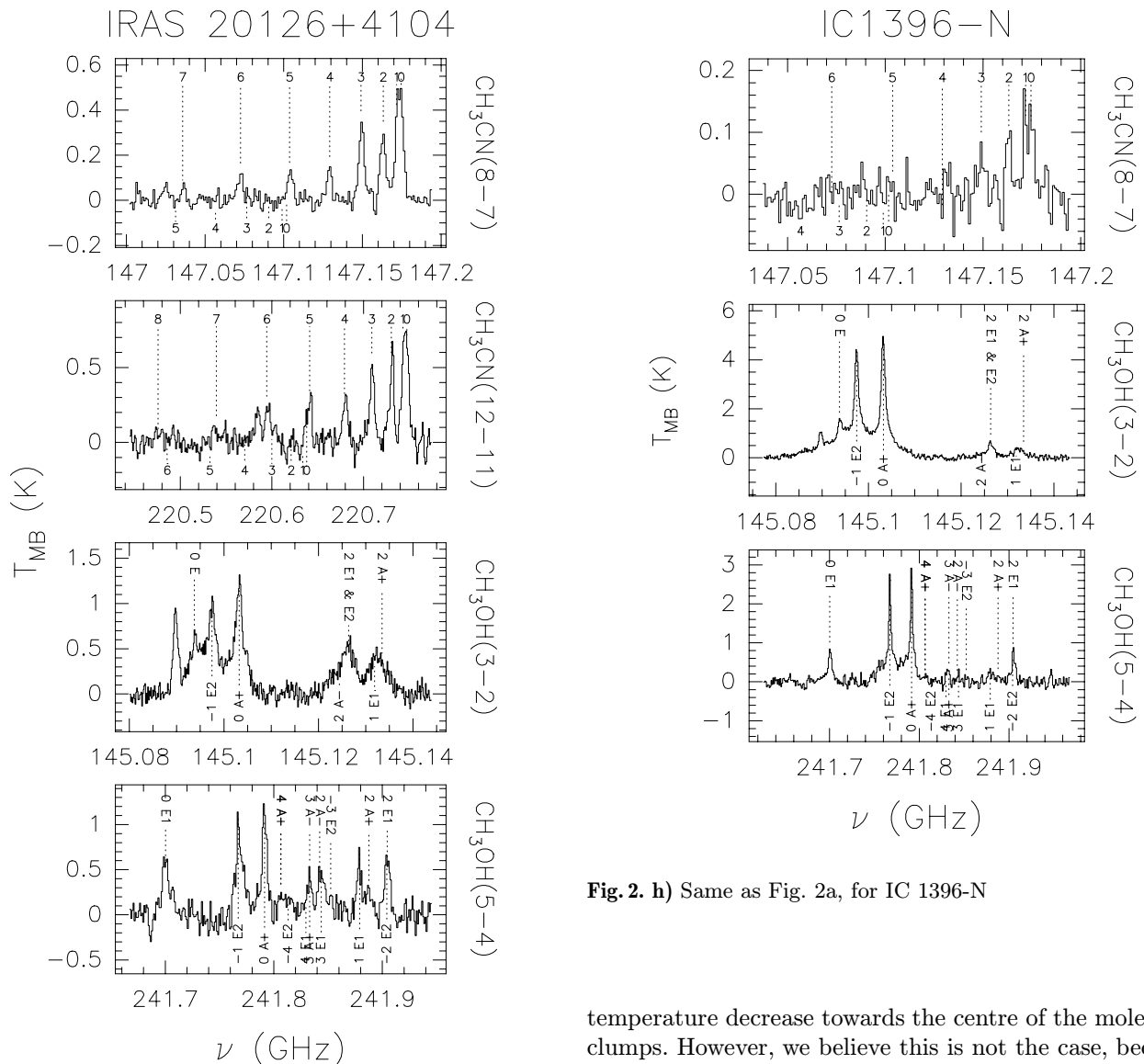


Fig. 2. g) Same as previous figure, for IRAS 20126+4104. Also the $\text{CH}_3\text{CH}_3\text{O}$ $7_{17} - 6_{06}$ line at 147024.8 MHz, the HNCO $10_{19} - 9_{18}$ line at 220584.766 MHz, and the C_3H_2 $3_{12} - 2_{21}$ line at 145089.63 MHz can be seen in the spectra

method, which assumes that the CH_3OH molecule is populated according to LTE. The corresponding Boltzmann plots are shown in Fig. 11 and the derived rotation temperatures and source averaged column densities are given in Table 12. We have assumed source angular diameters equal to those given in parentheses in Table 11.

One sees that, with the sole exception of IRAS 20126+4104, the values of T_{rot} are quite low, even lower than the peak brightness temperature of the $^{13}\text{CO}(2-1)$ line (see Table 7), which very likely represents just a lower limit to the kinetic temperature of the ^{13}CO gas. Since the CH_3OH gas is confined to a much smaller region than ^{13}CO (see Table 11), this might suggest a

Fig. 2. h) Same as Fig. 2a, for IC 1396-N

temperature decrease towards the centre of the molecular clumps. However, we believe this is not the case, because it is well known (see e.g. Johnston et al. 1992) that the CH_3OH molecule is subthermally excited, namely that T_{rot} underestimates the true CH_3OH kinetic temperature. Indeed, better temperature indicators such as CH_3CN give larger values of T_{rot} than CH_3OH , i.e. ~ 30 K for NGC 281-W and ~ 150 K for IRAS 20126+4104. Also, the latter source has been observed in the $\text{CH}_3\text{CN}(6-5)$ transition with high angular resolution (Cesaroni et al. 1997a), confirming the existence of a small ($\sim 1''$) dense core much hotter (~ 200 K) than the gas on larger scales, such as ^{13}CO and CH_3OH .

Unlike T_{rot} , the column density derived from CH_3OH is quite reliable. For an assumed CH_3OH abundance with respect to H_2 of 10^{-7} , one derives an H_2 column density of 10^{22} cm^{-2} , which is about an order of magnitude below the value derived for clumps associated with UC HII regions (Cesaroni et al. 1991). This result is consistent with the conclusion of Sect. 4.5 that the densities of our sample are lower than those derived by Cesaroni et al. (1991) for their clumps.

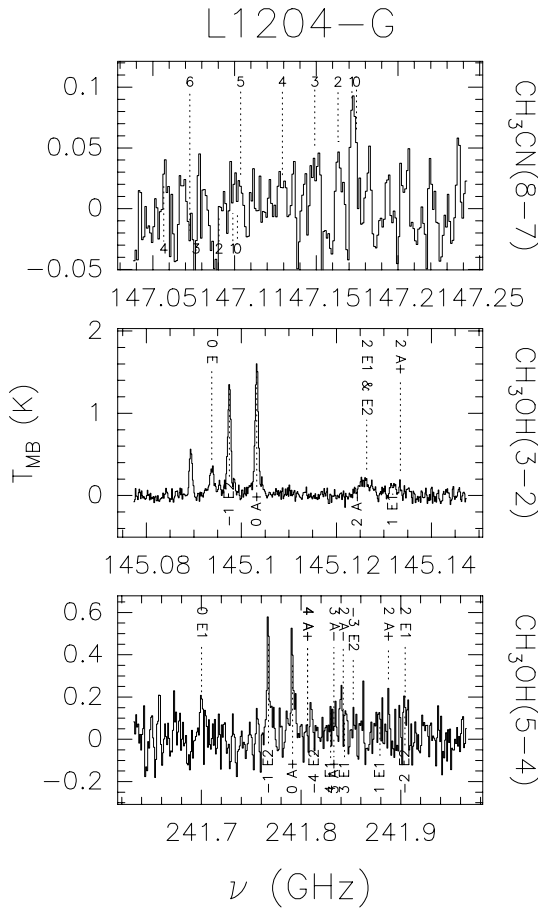


Fig. 2. i) Same as previous figure, for L1204-G

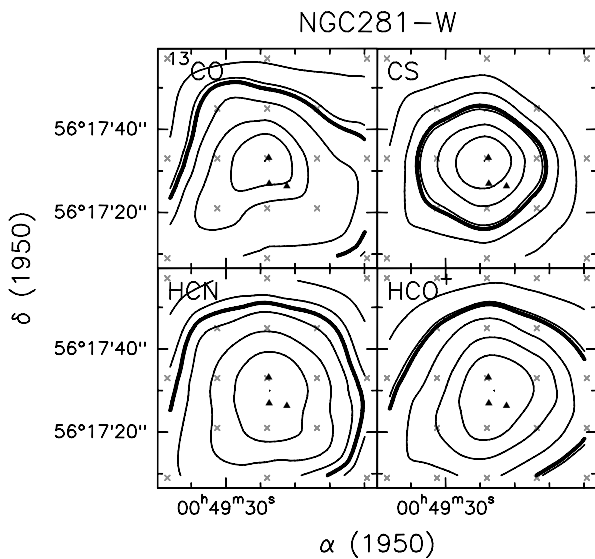


Fig. 3. a) Maps towards NGC 281-W of the integrated emission in the $^{13}\text{CO}(2-1)$ (top left panel), $\text{HCN}(1-0)$ (bottom left), $\text{CS}(3-2)$ (top right), and $\text{HCO}^+(1-0)$ (bottom right) lines. Thick contours correspond to 50% of the maximum in each map. The \times indicate the observed positions, and the filled triangles the positions of the H_2O maser spots. The values of the contour levels are given in Table 6

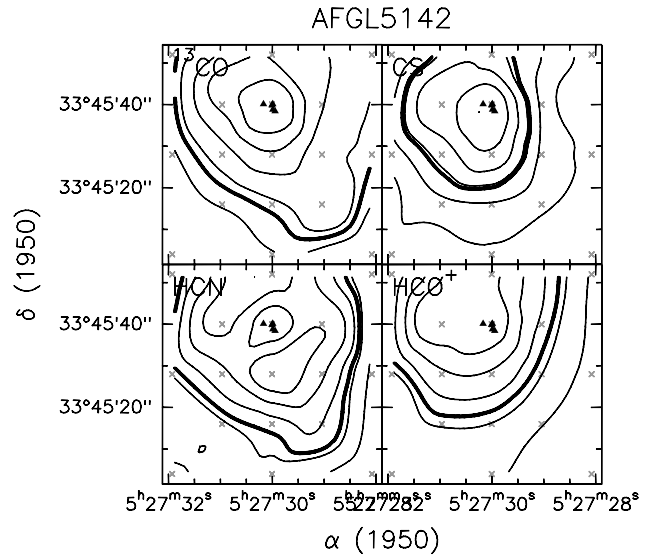


Fig. 3. b) Same as previous figure, for AFGL5142

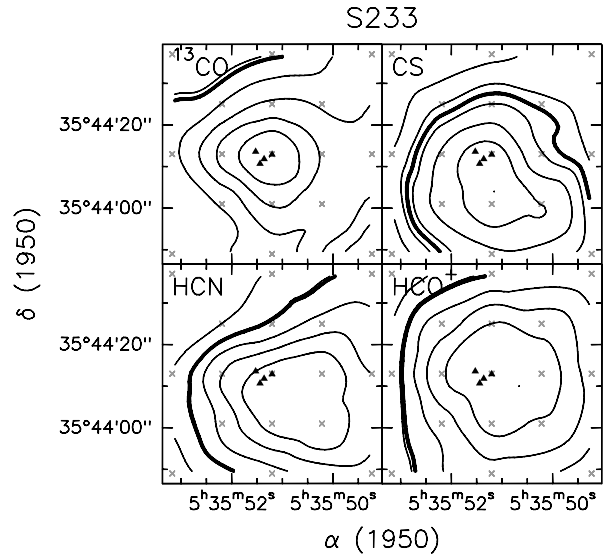


Fig. 3. c) Same as previous figure, for S233

5. Comments on individual sources

We now comment on the most interesting sources and compare with earlier work in the literature. We also present maps in selected velocity intervals in the $\text{HCO}^+(1-0)$ and $\text{CS}(3-2)$ lines aimed at detecting distinct components in the molecular cloud and, possibly, bipolar outflows.

5.1. NGC 281-W

NGC 281-W has been recently studied by Henning et al. (1994) as well as by Megeath & Wilson (1997), who have made detailed $\text{C}^{18}\text{O}(2-1)$, $\text{C}^{18}\text{O}(1-0)$, and $\text{C}^{34}\text{S}(3-2)$

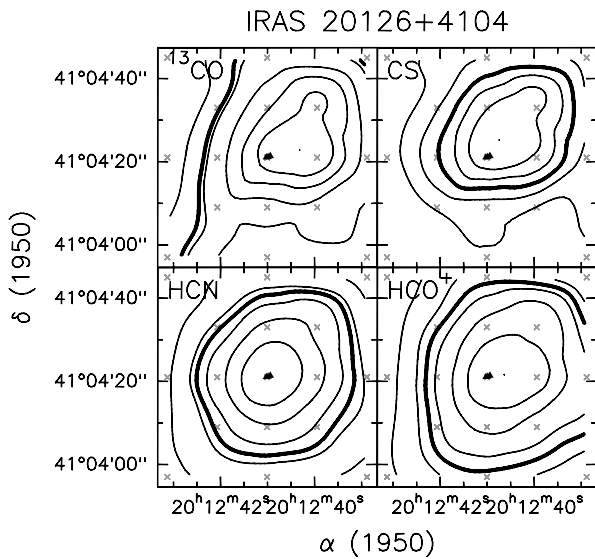


Fig. 3. d) Same as previous figure, for IRAS 20126+4104

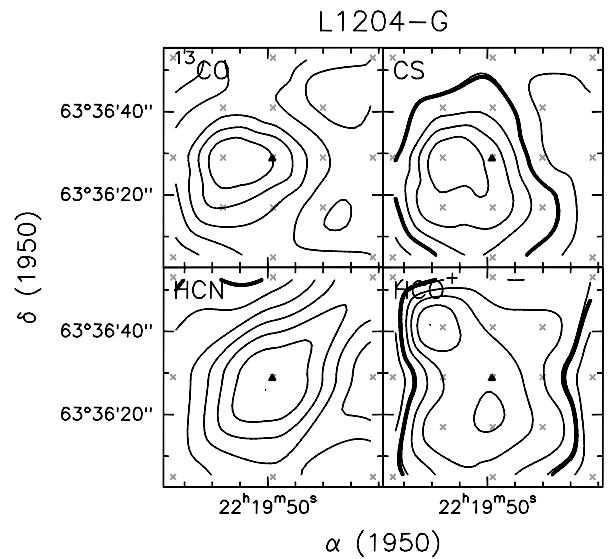


Fig. 3. f) Same as previous figure, for L1204-G

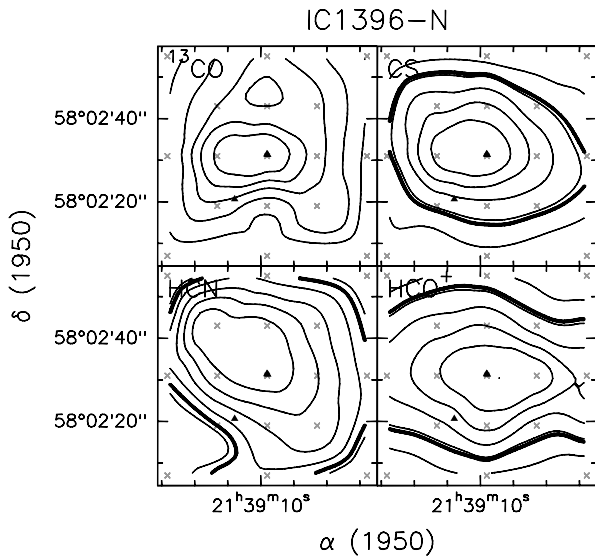


Fig. 3. e) Same as previous figure, for IC 1396-N

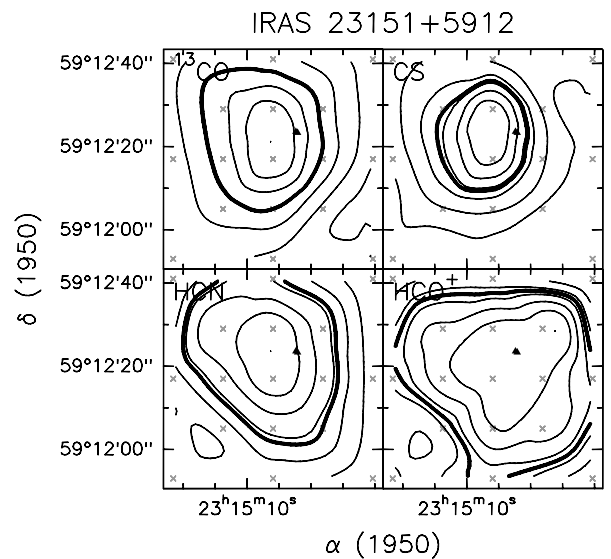


Fig. 3. g) Same as previous figure, for IRAS 23151+5912

maps of the clump studied by us, using the IRAM 30-m telescope. Our maps in the $C^{34}S(3-2)$ line are very similar to those obtained by Megeath and Wilson in the same transition, although our map is just sufficient to cover the $C^{34}S$ clump. From their $C^{18}O$ measurements, Megeath and Wilson derive a clump mass of at least $210 M_{\odot}$ and an H_2 column density of $5 \cdot 10^{22} \text{ cm}^{-2}$. Henning et al. (1994) detected a 1.3 mm continuum source coincident with the IRAS source. They concluded that the main contributor to this was a compact component of temperature 45 K and angular size $2'' - 3''$. They estimated the peak H_2 column density to be $2 \cdot 10^{23} \text{ cm}^{-2}$ or 4 times larger than the value from $C^{18}O$. This does not agree with our beam averaged estimate based upon ^{13}CO of $2 \cdot 10^{22} \text{ cm}^{-2}$, obtained assuming a ^{13}CO abundance relative to H_2 of

$1.1 \cdot 10^{-6}$ and a temperature of 29 K as done by Megeath & Wilson (1997); note that the latter is consistent with the T_{MB} of $^{13}CO(2-1)$ (see Table 7). The column density from ^{13}CO agrees instead with the value derived by Megeath and Wilson from $C^{18}O$. One can also estimate the column density from $C^{34}S$, assuming spherical symmetry and calculating the H_2 volume density with the LVG program mentioned in Sect. 4.5. This gives an H_2 density of $5 \cdot 10^5 - 1 \cdot 10^6 \text{ cm}^{-3}$, which implies a source averaged H_2 column density of $(5 - 9) \cdot 10^{23} \text{ cm}^{-2}$, where we have used a distance of 3.1 kpc for the sake of comparison with the results of Megeath and Wilson. This value compares well with that derived from the 1.3 mm continuum, which suggests that $C^{34}S$ is indeed confined to the densest core

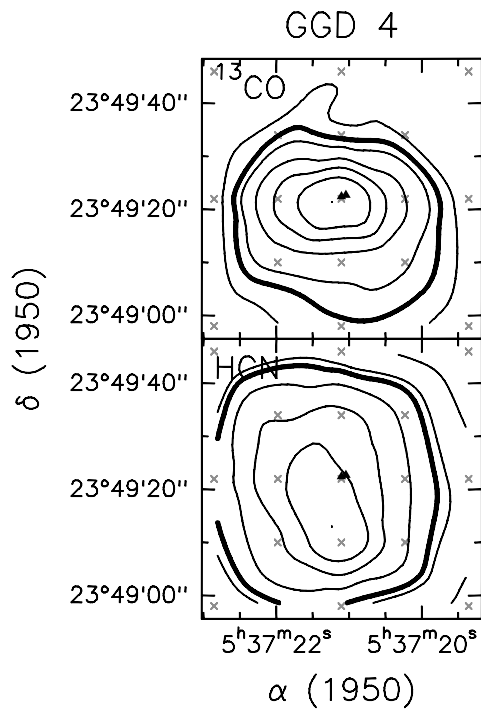


Fig. 4. a) Maps towards GGD 4 of the integrated emission in the $^{13}\text{CO}(2-1)$ (top panel) and $\text{HCN}(1-0)$ (bottom) lines. Thick contours correspond to 50% of the maximum in each map. The filled triangles indicate the positions of the H_2O maser spots, the \times the observed positions. The values of the contour levels are given in Table 6

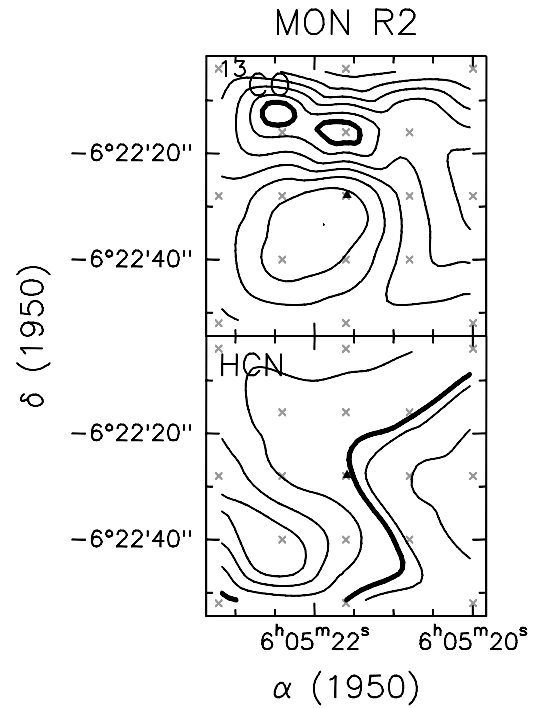


Fig. 4. c) Same as previous figure, for MON R2

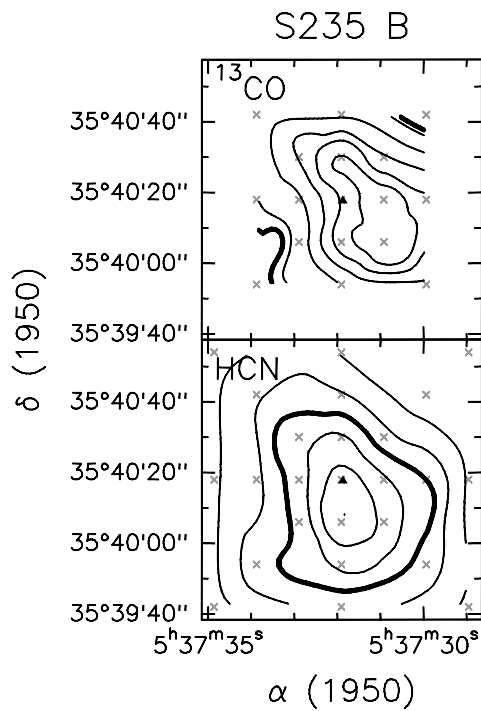


Fig. 4. b) Same as previous figure, for S235 B

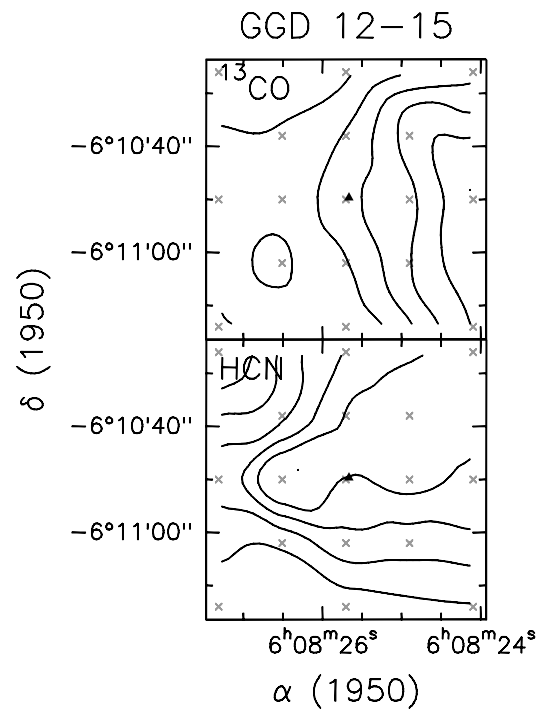


Fig. 4. d) Same as previous figure, for GGD 12-15

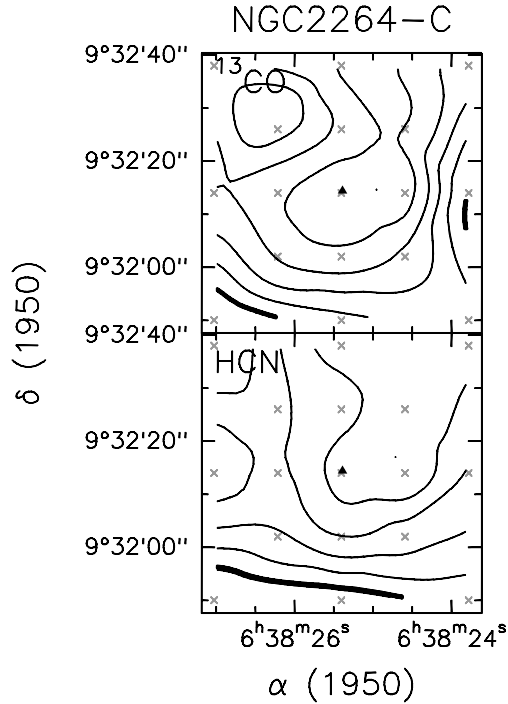


Fig. 4. e) Same as previous figure, for NGC 2264-C

associated with the H₂O maser and the FIR source seen by IRAS.

Henning et al. (1994) also mapped the source in CO(3–2) and found evidence of an E–W offset between the peaks of blue and red shifted emission (their Fig. 5). Snell et al. (1990) had previously detected the outflow in CO(1–0) using the FCRAO system and found no clear evidence for bipolarity. They derived an age of $2 \cdot 10^5$ yrs and a swept up mass of $11 M_{\odot}$ for the flow. Our data do not help much to clarify the situation. From Fig. 1a one sees that the line profiles towards NGC 281-W are quite complex: while the CS and ¹³CO lines peak at the bulk velocity given by C³⁴S, the HCO⁺ and HCN lines peak at lower velocities than C³⁴S. Moreover, another component is clearly visible in the red wing of the ¹³CO, HCO⁺, and CS transitions at ~ -28 km s⁻¹. Finally, broad line wings are evident even in the C³⁴S(3–2) line. Notwithstanding such a complexity of the line profile, the spatial distribution of the gas at different velocities looks quite the same, as the emission arises mostly from a region surrounding the H₂O masers. The sole exception is given by the gas associated with the line wings, namely from -42.0 to -36 km s⁻¹ and from -26 to -20 km s⁻¹, which seem to trace a bipolar outflow approximately centred on the H₂O maser and extending in the NE–SW direction. This is shown in Fig. 12 for the HCO⁺(1–0) line. In conclusion, it is quite difficult to decouple the different components which overlap in space and – at least in part – in velocity: high angular resolution images might help to identify the

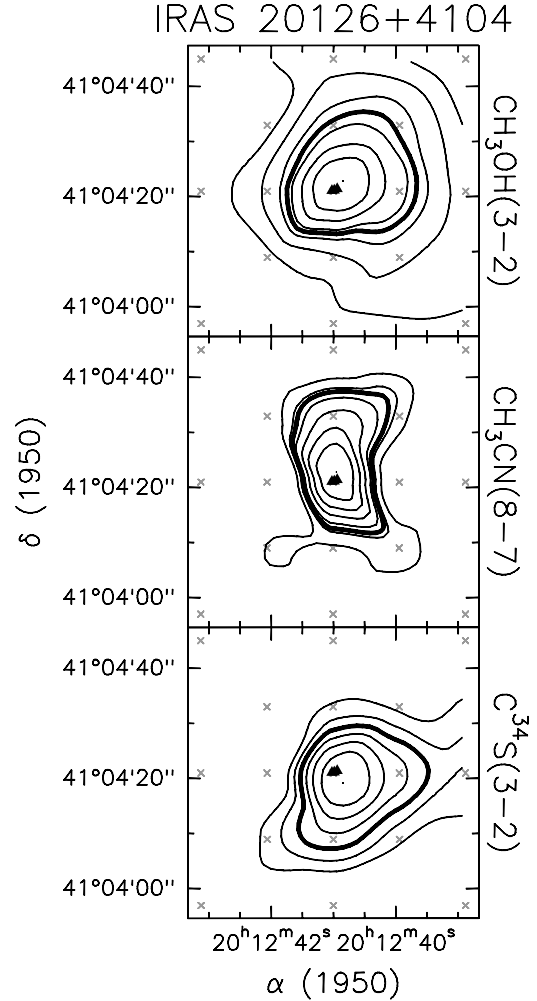


Fig. 5. Maps towards IRAS 20126+4104 of the integrated bulk emission in the CH₃OH(3–2) (top panel), CH₃CN(8–7) (middle), and C³⁴S(3–2) (bottom) transitions. Thick contours correspond to 50% of the maximum in each map. The HPBW is $\sim 17''$. The filled triangles indicate the positions of the H₂O maser spots, the × the observed positions. Contour levels for CH₃CN(8–7) range from 4.9 to 14 by 1.5 K km s⁻¹; the values of the contour levels for the other maps are given in Table 6

main centres of activity in the region and to describe their interaction with the surrounding environment.

5.2. AFGL5142

Two velocity components are present in this region, as clearly shown by the spectra of Fig. 1b: these are at ~ -4.3 km s⁻¹ and ~ -2.2 km s⁻¹. Looking at the C³⁴S map of Fig. 8 one sees that the emission peaks $\sim 12''$ south of the H₂O maser position, with a small extension towards the latter. Indeed, maps of the CS(3–2) emission in the core of the line, integrated from -7 to -3 km s⁻¹ and from -3 to 1 km s⁻¹, (see Fig. 13) reveal the existence of two clumps, one (to the south) at the C³⁴S peak position,

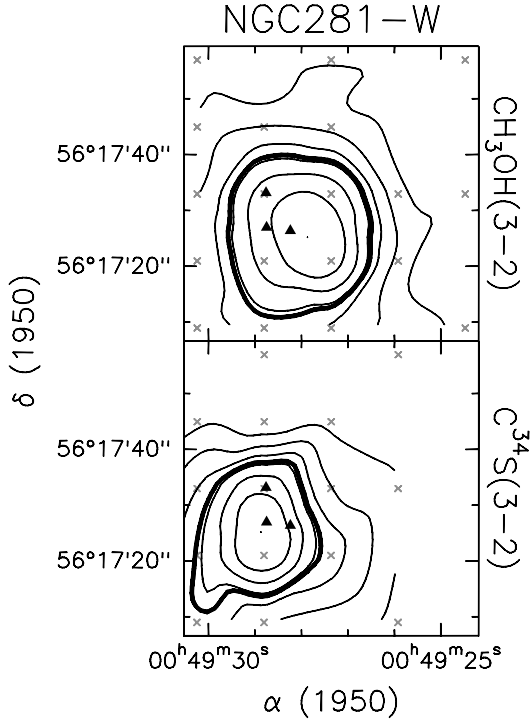


Fig. 6. Maps towards NGC 281-W of the integrated bulk emission in the $\text{CH}_3\text{OH}(3-2)$ (top panel) and $\text{C}^{34}\text{S}(3-2)$ (bottom) transitions. Thick contours correspond to 50% of the maximum in each map. The HPBW is $\sim 17''$. The filled triangles indicate the positions of the H_2O maser spots, the \times the observed positions. The values of the contour levels are given in Table 6

the other (to the north) associated with the H_2O masers. The northern clump is traced by all molecules observed, as proved by the maps in Fig. 3b, whereas the southern clump is seen only in C^{34}S and CS. Interestingly, the HCO^+ emission in the high velocity wings (i.e. from -19.5 to -7 km s^{-1} and from 1 to 15 km s^{-1}) peaks approximately at the position of the H_2O masers (see Fig. 14): this may indicate a bipolar outflow seen pole-on. We note that the HCO^+ outflow that we see in our map is in a direction different from that found in the $\text{CO}(2-1)$ line on a much larger scale (Hunter et al. 1995), but is consistent with that observed in the $\text{CO}(3-2)$ line with a similar resolution and on the same scale (Hunter et al. 1995).

In conclusion, one can speculate that in comparison with the “quiescent” southern clump, the northern clump is in a more advanced phase of the star formation process, characterised by various signposts of activity such as the H_2O masers and a small scale molecular outflow.

5.3. S233

The spectra of Fig. 1c clearly indicate two velocity components, corresponding to the approximate velocity ranges from -17 to -13.5 km s^{-1} and from -20.5 to -17 km s^{-1} . In Fig. 15 we show the maps of the $\text{CS}(3-2)$ line

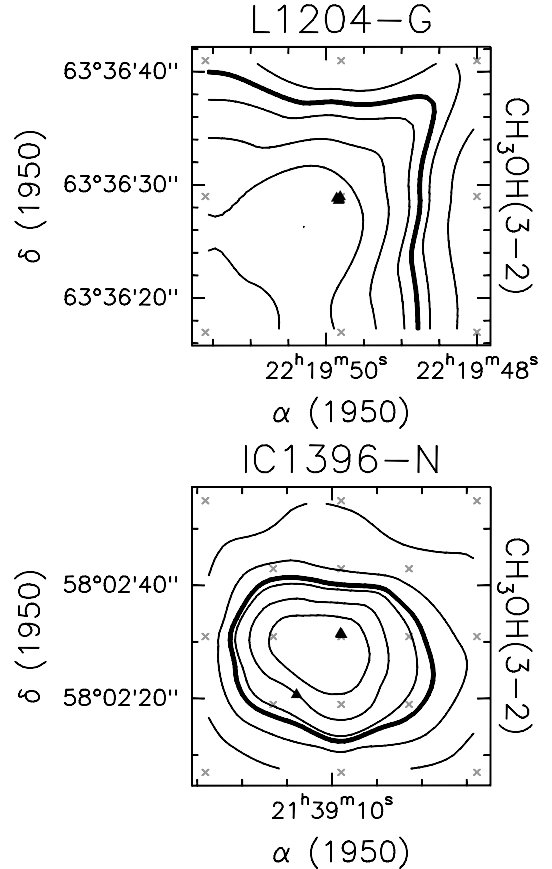


Fig. 7. Maps towards IC 1396-N and L1204-G of the integrated bulk emission in the $\text{CH}_3\text{OH}(3-2)$ transitions. Thick contours correspond to 50% of the maximum in each map. The HPBW is $\sim 17''$. The filled triangles indicate the positions of the H_2O maser spots, the \times the observed positions. The values of the contour levels are given in Table 6

emission integrated in these velocity intervals: two molecular clumps are evident, one at the H_2O maser position, the other offset to the south-west. The same pattern is seen in the other transitions, with the sole exception of C^{34}S , which traces only the H_2O maser clump, as is evident from Fig. 8: this proves that the latter clump is denser than the other, consistent with the idea that star formation is going on in it.

5.4. S235 B

The $\text{C}^{34}\text{S}(2-1)$, $(3-2)$, $(5-4)$ and $^{13}\text{CO}(2-1)$ observations around the highly variable H_2O maser located between the S235 A and B optical nebulosities, together with near infrared broad band (J , H and K) and narrow band (H_2 S(1) $1\rightarrow 0$ and $\text{Br}\gamma$) images were discussed in Felli et al. (1997).

A highly obscured stellar cluster is present between the thermal radio components S235 A and B in the near IR observations. The colour-colour analysis shows that the

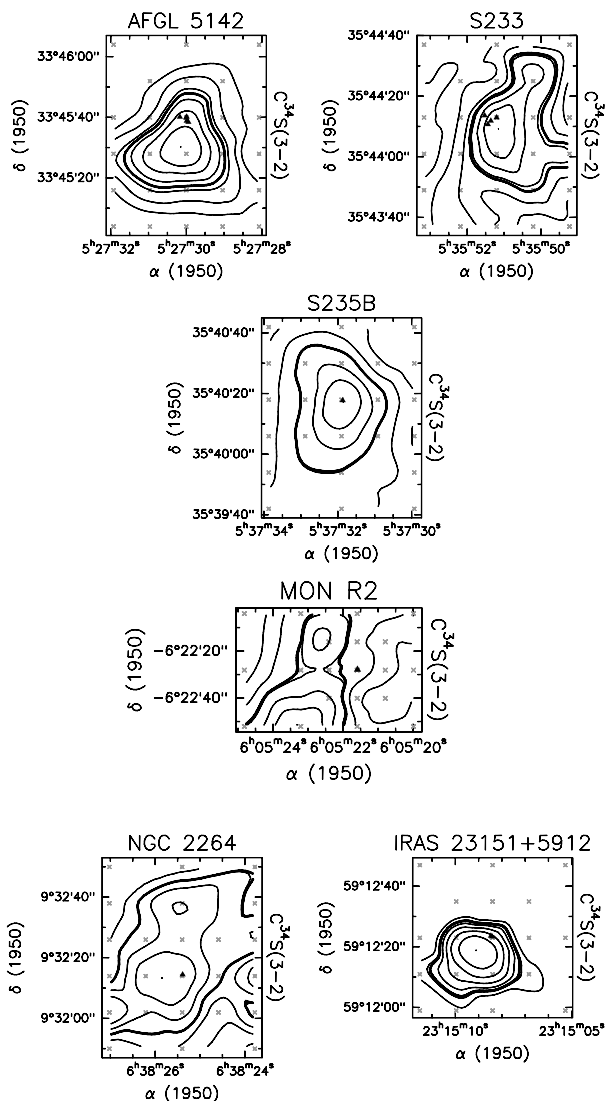


Fig. 8. Same as Fig. 7 for the $C^{34}S(3-2)$ line towards AFGL5142, S233, S235 B, MON R2, NGC 2264-C, and IRAS23151+5912. Thick contours correspond to 50% of the maximum in each map. The HPBW is $\sim 17''$. The filled triangles indicate the positions of the H_2O maser spots, the \times the observed positions. The values of the contour levels are given in Table 6

cluster contains many sources with infrared excess, most probably YSOs in an early evolutionary stage.

The driving source of the H_2O maser does not appear to be either the YSO inside S235 A or S235 B, but is identified with a faint near infrared member of the cluster, with a large ($H - K$) colour excess, located near the position of the maser. This identification is further supported by the coincidence of the maser and the near IR source with the centre of the high density and hot compact molecular core observed in $C^{34}S$ and ^{13}CO . The lack of radio continuum emission from the maser/near IR source suggests that the YSO powering the maser and responsible

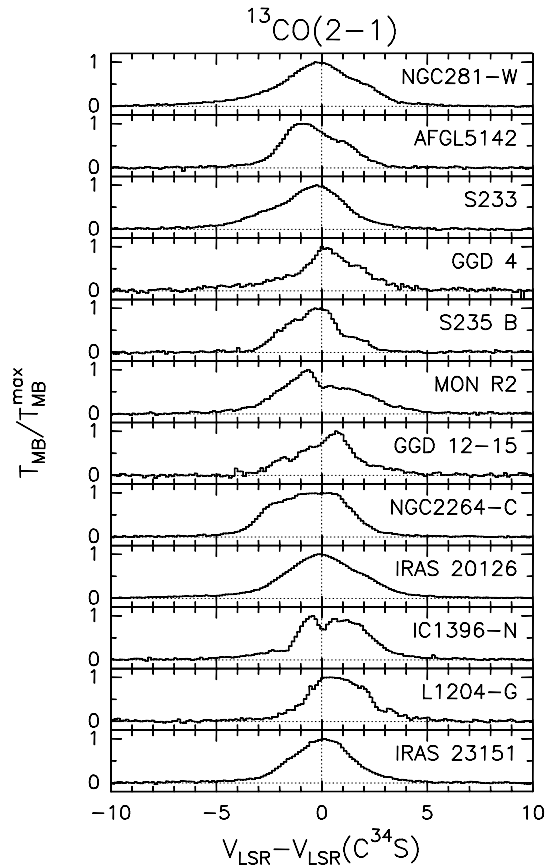


Fig. 9. Spectra of the $^{13}CO(2-1)$ line towards the peak position in each map. The velocity on the abscissa is relative to the V_{LSR} of the corresponding $C^{34}S(3-2)$ line. The intensity is normalised with respect to the peak of each spectrum

for the near IR emission must be in a very early evolutionary stage, highly obscured even at K band and strongly self-absorbed in the radio continuum, in any case much younger than S235 A and S235 B. S235 A and S235 B lie on the sides of the molecular core, suggesting that star formation in the complex is not coeval but proceeds from the outside towards the core of the molecular cloud.

As far as the CO outflow reported by Nakano & Yoshida (1986), the blue-shifted lobe from -24 km s^{-1} to -20 km s^{-1} can be seen also in the $^{13}CO(2-1)$ data (see Fig. 4 of Felli et al. 1997) and is located between the H_2O maser and S235 B. However, the red-shifted lobe observed in ^{12}CO from -13 to -6 km s^{-1} (which is also weaker in Nakano & Yoshida 1986) was not detected in our data. The red wing of the ^{12}CO profile may be affected by a superposition of different velocity components south of S235 B and has been questioned by Snell et al. (1990) and by Nakano & Yoshida (1986) themselves. Consequently, the earlier suggestion that S235 B was the source of the outflow is questionable and the possibility that the blue outflow comes from the H_2O maser must be retained as a plausible alternative.

Table 6. Values of contours in Figs. 3 to 8. The three numbers in each entry of the table represent the minimum level, the maximum level, and the step in K km s⁻¹

Source	¹³ CO(2 – 1) (K km s ⁻¹)	HCN(1 – 0) (K km s ⁻¹)	HCO ⁺ (1 – 0) (K km s ⁻¹)	CS(3 – 2) (K km s ⁻¹)	C ³⁴ S(3 – 2) (K km s ⁻¹)	CH ₃ OH(3 – 2) (K km s ⁻¹)
NGC 281-W	24.7; 126.4; 17.0	7.6; 49.7; 7.0	8.3; 37.8; 4.9	4.5; 65.9; 10.2	0.6; 7.6; 1.2	6.5; 86.6; 13.3
AFGL5142	38.2; 106.0; 13.6	12.5; 69.6; 9.5	10.2; 50.1; 8.0	5.1; 77.7; 12.1	1.3; 7.9; 1.1	—
S233	37.3; 98.5; 10.2	12.7; 46.5; 6.8	13.3; 58.1; 7.5	7.8; 54.4; 7.8	0.5; 6.3; 0.97	—
GGD 4	17.8; 48.3; 6.1;	5.3; 28.0; 3.8	—	—	—	—
S235B	54.8; 126.5; 11.9	0.4; 66.9; 11.1	—	—	0.12; 10.6; 1.7	—
MON R2	76.9; 163.8; 14.5	11.3; 48.4; 7.4	—	—	0.21; 6.5; 1.1	—
GGD 12-15	54.6; 99.5; 7.5	27.2; 44.8; 2.9	—	—	—	—
NGC 2264	53.6; 135.2; 13.6	26.2; 68.0; 7.0	—	—	0.07; 6.4; 1.1	—
IRAS 20126+4104	39.9; 139.8; 16.6	11.5; 67.7; 9.4	9.6; 66.2; 9.4	8.0; 47.9; 8.0	1.0; 3.7; 0.52	3.3; 26.0; 3.8
IC 1396-N	60.3; 99.6; 7.8	18.1; 45.4; 5.5	9.3; 33.0; 4.0	16.6; 51.5; 7.0	—	7.2; 59.9; 10.5
L1204-G	40.4; 59.8; 3.9	5.9; 12.2; 1.1	4.8; 17.2; 2.1	3.4; 12.1; 1.8	—	1.7; 11.4; 1.6
IRAS 23151+5912	2.3; 115.1; 18.8	1.7; 20.0; 3.1	1.3; 8.8; 1.3	2.4; 23.9; 4.3	1.1; 2.8; 0.3	—

5.5. NGC 2264-C

An extensive molecular and IR study of the source was presented by Schreyer et al. (1997), who mapped a much larger region than in our study. They observed many different transitions, of which only the CS(3 – 2) and C³⁴S(3 – 2) lines are in common with us: for these, our results are consistent with those of Schreyer et al. (1997). In particular, the emission peaks at the position of the H₂O masers rather than at the IR source IRS1. Moreover, the secondary clump identified by Schreyer et al. to the south-east of IRS1 can be partially seen also in our C³⁴S(3 – 2) map of Fig. 8, although at the very edge of it. However, the existence of this clump at a velocity of ~ 6.2 km s⁻¹ is clearly demonstrated by the ¹³CO and HCN line profiles of Fig. 1h. Unfortunately, we cannot confirm the molecular outflows seen by Schreyer et al. because for this source we do not have maps in CS and HCO⁺, and ¹³CO and HCN are not suitable for investigating the line wings. In fact, ¹³CO arises from a much larger region than that mapped by us, while study of HCN emission is complicated by the hyperfine structure of the line.

5.6. IRAS 20126+4104

Our Pico Veleta observations as well as Plateau de Bure interferometer (PdBI) maps of the molecular gas and near infrared images of the same region, were presented in Cesaroni et al. (1997a).

All lines peak at ~ -3.5 km s⁻¹ and the lower density tracers like ¹³CO or HCO⁺ present broad wings extending up to ~ 24 km s⁻¹ from the peak. Even the higher density tracer C³⁴S, despite the much poorer S/N, shows strong wings, although only up to ~ 6 km s⁻¹ from the peak. On this basis, five velocity ranges were defined:

- the *bulk emission* (from -5 to -2 km s⁻¹), which corresponds to the narrow component of the C³⁴S(3 – 2) line;
- the *inner wings* (from -9 to -5 km s⁻¹ and from -2 to 2 km s⁻¹), also clearly visible in the C³⁴S(3 – 2) line;
- the *outer wings* (from -28 to -9 km s⁻¹ and from 2 to 21 km s⁻¹), seen in the HCO⁺(1 – 0), ¹³CO(2 – 1), HCN(1 – 0), and CS(3 – 2) lines.

The bulk emission is best studied through the high density tracers such as the CH₃OH(3 – 2), CH₃CN(8 – 7), and C³⁴S(3 – 2) transitions. In all cases the emission originates from the same region with size $\sim 15''$, centred on the H₂O maser spots: this is a clear indication of the existence of a molecular clump in which the IRAS source and the H₂O masers are embedded.

In order to map the line wings, one has to use the lines with the best S/N, such as CS(3 – 2) and HCO⁺(1 – 0) (see Fig. 4 of Cesaroni et al. 1997a). The outer wings seem to trace a NW–SE velocity shift, with the blue- and red-shifted emission coming respectively from NW and SE. The surprising result is that the blue- and red-shifted emission in the inner wings shows an orientation completely reversed with respect to the NW–SE axis above: although the direction is the same, the velocity increases from SE to NW.

Including the interferometric observations made with the PdBI, the main results are the following:

1. IRAS 20126+4104 is embedded in a molecular clump seen in all tracers, which is centred on the H₂O masers position and is ~ 0.16 pc large; its temperature and mass are ~ 50 K and $\sim 150 M_{\odot}$.
2. A bipolar outflow seen in the HCO⁺(1 – 0) and CS(3 – 2) lines arises from the centre of the clump and extends on a scale of ~ 0.25 pc. The H₂O maser

Table 7. Line parameters at centre position

Line	V_{\min} (km s ⁻¹)	V_{\max} (km s ⁻¹)	T_{MB} (K)	V_{LSR} (km s ⁻¹)	$FWHM$ (km s ⁻¹)	$\int T_{\text{MB}}dV$ (K km s ⁻¹)	RMS (K)
NGC 281-W							
¹³ CO(2 – 1)	–39.0	–24.6	27.1	–30.6	4.0	125.7	0.3
HCO ⁺ (1 – 0)	–44.0	–9.5	7.9	–31.1	3.0	36.8	0.052
CS(3 – 2)	–51.0	–13.0	11.7	–30.7	4.2	65.3	0.11
C ³⁴ S(2 – 1)	–36.0	–20.0	0.4	–30.0	3.3	1.3	0.22
C ³⁴ S(3 – 2)	–37.0	–23.0	1.6	–30.5	3.5	6.3	0.19
C ³⁴ S(5 – 4)	–39.0	–23.0	1.3	–31.5	3.6	4.8	0.6
HCN(1 – 0)	–52.4	–13.0	5.9	–31.3	3.2	48.5	0.065
AFGL5142							
¹³ CO(2 – 1)	–8.0	0.5	26.1	–4.1	3.5	91.3	0.3
HCO ⁺ (1 – 0)	–19.5	15.0	9.1	–4.4	4.5	41.0	0.21
CS(3 – 2)	–24.0	9.0	12.9	–4.2	4.4	63.1	0.11
C ³⁴ S(2-1)	–10.0	5.0	0.75	–2.6	3.3	2.7	0.17
C ³⁴ S(3 – 2)	–12.0	7.5	1.5	–2.2	4.1	6.5	0.27
C ³⁴ S(5 – 4)	–9.0	5.0	0.8	–2.1	2.5	3.0	1.0
HCN(1 – 0)	–20.4	21.3	7.5	–4.7	3.1	65.8	0.057
S233							
¹³ CO(2 – 1)	–23.6	–10.5	23.8	–16.0	3.5	98.3	0.3
HCO ⁺ (1 – 0)	–38.5	10.0	11.2	–15.2	3.7	57.1	0.060
CS(3 – 2)	–30.0	0.0	11.7	–15.0	2.9	50.0	0.099
C ³⁴ S(2 – 1)	–28.0	–5.0	0.4	–16.1	2.3	0.9	0.19
C ³⁴ S(3 – 2)	–21.0	–9.0	1.9	–15.7	3.0	5.9	0.27
C ³⁴ S(5 – 4)	–27.0	–3.0	0.8	–15.7	5.6	4.7	1.1
HCN(1 – 0)	–31.0	2.0	5.1	–15.4	3.1	49.1	0.060
GGD 4							
¹³ CO(2 – 1)	–4.5	7.0	14.8	1.8	3.0	53.8	0.45
C ³⁴ S(2 – 1)			<1.8				0.6
C ³⁴ S(3 – 2)	–2	7.0	0.7	1.7	2.7	1.75	0.3
C ³⁴ S(5 – 4)			<3				1.0
HCN(1 – 0)	–8.5	16.9	4.6	1.9	1.9	24.6	0.060

spots are aligned along the axis of the outflow. Its mass loss rate, momentum, and mechanical luminosity are large, suggesting it to arise from a young active stellar object in an early and active stage of its formation.

3. The NIR continuum and H₂ line emission looks elongated in the same direction as the bipolar structure seen in HCO⁺ at high angular resolution, thus confirming the interpretation of this as a bipolar outflow ejected from a central source coincident with the nominal position of IRAS 20126+4104.
4. The high density tracers like CH₃CN map a dense compact core of diameter ~ 0.0082 pc centred on the H₂O masers, with temperature ~ 200 K and mass $\sim 10 M_{\odot}$. Although only barely resolved, we find evidence for such core being elongated in a direction perpendicular to the outflow axis and subject to a velocity field which we interpret as rotation around that axis.

In summary, IRAS 20126+4104 represents a rare beautiful example of a disk-outflow system originating from a young early type massive (proto)star still in an evolutionary phase prior to the development of an UC HII region.

5.7. IC 1396-N

The IC 1396-N (or IC 1396E) globule has been studied in detail by Serabyn et al. (1993) using molecular line data taken with the Effelsberg 100-m, the IRAM 30-m, and the CSO 10.4-m telescopes. In particular, they obtained maps in CS(3 – 2) which well compare with ours, although the region mapped by them is larger. They determined the mass of the globule to be $480 M_{\odot}$ within an outer radius of 0.9 pc and with a density distribution varying as $r^{-1.75}$. From the ammonia measurements,

Table 7. continued

Line	V_{\min} (km s ⁻¹)	V_{\max} (km s ⁻¹)	T_{MB} (K)	V_{LSR} (km s ⁻¹)	$FWHM$ (km s ⁻¹)	$\int T_{\text{MB}}dV$ (K km s ⁻¹)	RMS (K)
S235 B							
¹³ CO(2 – 1)	–20.9	–13.3	32.9	–17.1	2.9	99.7	0.5
C ³⁴ S(2 – 1)	–22.0	–10.0	1.5	–16.8	2.3	3.7	0.15
C ³⁴ S(3 – 2)	–21.0	–13.0	4.3	–17.1	2.2	10.5	0.26
C ³⁴ S(5 – 4)	–21.0	–9.0	2.1	–17.0	2.6	5.9	0.7
HCN(1 – 0)	–40.0	17.4	12.2	–17.2	2.3	63.5	0.048
MONR2							
¹³ CO(2 – 1)	3.1	17.0	38.2	9.8	4.0	153.6	0.9
C ³⁴ S(2 – 1)	6.0	16.0	0.4	10.7	2.4	1.0	0.17
C ³⁴ S(3 – 2)	6.0	14.5	1.3	10.5	2.5	3.5	0.27
C ³⁴ S(5 – 4)	6.2	13.0	1.2	9.7	1.2	1.6	0.6
HCN(1 – 0)	–0.5	23.1	5.7	9.8	1.4	29.0	0.071
GGD 12-15							
¹³ CO(2 – 1)	8.3	16.6	23.7	12.5	2.8	74.7	0.8
C ³⁴ S(2 – 1)	7.0	16.0	0.8	11.9	2.4	1.4	0.17
C ³⁴ S(3 – 2)	8.0	15.0	2.4	11.8	2.5	3.3	0.27
C ³⁴ S(5 – 4)			<0.9				0.3
HCN(1 – 0)	–1.3	22.3	8.0	12.0	2.2	41.8	0.066
NGC 2264-C							
¹³ CO(2 – 1)	2.5	13.7	27.7	8.4	4.7	133.6	0.3
C ³⁴ S(2 – 1)	0.0	16.0	0.9	8.2	3.4	3.5	0.26
C ³⁴ S(3 – 2)	3.5	13.5	2.4	8.4	2.5	6.3	0.35
C ³⁴ S(5 – 4)			<0.9				0.3
HCN(1 – 0)	–6.0	28.2	9.3	9.1	3.7	63.4	0.056

they determined the temperature to be 20 – 23 K. With this model, they predicted an intensity of 1.6 – 1.9 K for C³⁴S(3 – 2) with the 30-m or 35% larger than our observed value of 1.3 K. They find the wing emission (–7.25 to –1.25 km s⁻¹ and 2.75 to 8.75 km s⁻¹) to be localised around the water maser source whereas the bulk emission (i.e. from –1.25 to 2.75 km s⁻¹) is more extended. Indeed our results are quite consistent with this view. However, in their Fig. 5 Serabyn et al. present the CS(3 – 2) line emission integrated under both line wings: if one instead compares the emission in the blue wing with that in the red, an offset in the E–W direction between the two is found. This is shown in Fig. 16, where the same velocity intervals as in Fig. 5 of Serabyn et al. (1993) have been used. Note that such an offset and orientation is also found in an interferometric map of the HCO⁺(1 – 0) emission (Testi, private communication). One possibility is that the structure outlined in Fig. 16 is a bipolar flow, although it should be noted that only the blue lobe is peaked at the centre position, namely where the bulk CS(3 – 2) emission peaks. Whatever the interpretation, the structure of the molecular cloud in this source is not as simple as assumed by Serabyn et al. (1993). Although to a first

approximation one can make the hypothesis of a single homogeneous clump, in practice the line profiles shown in Fig. 1j demonstrate that sub-structures must exist, and temperature and density gradients must play an important role – as witnessed e.g. by the self-absorption features in the HCO⁺ line.

5.8. IRAS 23151+5912

In this source the H₂O masers are slightly offset from the peak of the C³⁴S emission (see Fig. 8), although likely embedded in the C³⁴S clump. By inspection of Fig. 11, one sees that two velocity components are detected in the HCO⁺(1 – 0) and, perhaps, HCN(1 – 0) lines. Indeed, the region mapped in these transitions looks more extended than that seen in CS or ¹³CO (see Fig. 3g). The complexity of the molecular cloud is better evidenced by separating the contribution of the two velocity components in the HCO⁺ line. This is done in Fig. 17 where the distribution of the HCO⁺ line emission integrated from –60 to –55 km s⁻¹ is compared with that from –55 to –48 km s⁻¹. Figure 17 seems to outline two clumps, neither of which can be safely associated with the H₂O

Table 7. continued

Line	V_{\min} (km s ⁻¹)	V_{\max} (km s ⁻¹)	T_{MB} (K)	V_{LSR} (km s ⁻¹)	$FWHM$ (km s ⁻¹)	$\int T_{\text{MB}}dV$ (K km s ⁻¹)	RMS (K)
IRAS 20126+4104							
¹³ CO(2 – 1)	–10.9	2.5	29.7	–3.6	4.4	129.2	0.45
HCO ⁺ (1 – 0)	–67.6	40.7	13.2	–3.5	3.4	65.4	0.050
CS(3 – 2)	–21.0	14.0	10.0	–3.7	3.2	44.5	0.11
C ³⁴ S(2 – 1)	–6.5	4.5	0.2	–3.2	4.4	0.6	0.06
C ³⁴ S(3 – 2)	–12.0	8.0	0.7	–3.6	4.2	4.4	0.22
C ³⁴ S(5 – 4)	–15.0	15.0	0.7	–2.7	8.1	5.4	0.22
HCN(1 – 0)	–24.8	18.4	9.6	–3.6	2.7	67.6	0.070
IC 1396-N							
¹³ CO(2 – 1)	–5.4	7.6	26.0	–0.2	3.7	106.7	0.6
HCO ⁺ (1 – 0)	–48.0	40.0	8.5	–0.5	1.3	32.9	0.048
CS(3 – 2)	–23.0	29.0	10.9	–0.1	3.4	57.2	0.11
C ³⁴ S(2 – 1)	–6.0	12.0	0.76	0.8	3.7	2.9	0.21
C ³⁴ S(3 – 2)	–6.0	6.5	1.3	0.3	3.0	4.0	0.31
C ³⁴ S(5 – 4)			<3.0				1.0
HCN(1 – 0)	–26.9	34.1	6.0	–0.4	1.4	47.9	0.068
L1204-G							
¹³ CO(2 – 1)	–17.2	–6.1	17.7	–10.8	3.3	62.0	0.5
HCO ⁺ (1 – 0)	–26.5	7.5	4.1	–11.3	2.5	14.7	0.043
CS(3 – 2)	–21.9	–2.5	3.2	–10.5	2.4	11.3	0.11
C ³⁴ S(2 – 1)	–12.7	–9.3	0.6	–11.0	1.1	0.7	0.18
C ³⁴ S(3 – 2)	–16.0	–5.0	0.5	–11.8	3.2	3.0	0.27
C ³⁴ S(5 – 4)			<0.4				0.13
HCN(1 – 0)	–22.7	–2.6	2.1	–11.6	3.0	12.1	0.061
IRAS 23151+5912							
¹³ CO(2 – 1)	–59.3	–49.0	29.5	–54.0	3.4	108.4	0.7
HCO ⁺ (1 – 0)	–75.0	–30.0	1.5	–54.0	4.5	8.2	0.039
CS(3 – 2)	–65.0	–47.0	7.8	–54.1	2.6	24.9	0.10
C ³⁴ S(2 – 1)	–56.5	–52.7	0.3	–54.5	1.3	0.4	0.11
C ³⁴ S(3 – 2)	–60.0	–49.5	0.7	–54.5	3.0	2.4	0.21
C ³⁴ S(5 – 4)			<0.3				0.1
HCN(1 – 0)	–67.1	–43.0	2.8	–54.0	3.3	17.9	0.076

maser spots. Under this respect IRAS 23151+5912 differs from all the other sources. Clearly, the situation is more complex in this case: a tentative explanation may be that the H₂O masers are located in a high density region at the interface between the two clumps. Any further speculation will require higher angular resolution data.

6. Outline of main results

Our sample of IRAS sources contains objects with a wide range of bolometric luminosity and we have therefore examined our data for correlations between the various quantities measured. When doing this, one should bear in mind the fact that the different molecular tracers

sample gas of greatly differing properties. For example, the measured linewidths show that the HCN(1 – 0) and HCO⁺(1–0) lines are in large part formed in the outflows. The compactness of the methyl cyanide emission together with the high excitation temperatures shows that CH₃CN traces dense gas close to the IRAS source. At least in the case of IRAS 20126+4104 (Cesaroni et al. 1997a), there is evidence that the methyl cyanide emission comes from a disk like structure at distances of around 1000 AU from the young star.

The effectiveness of HCO⁺ and HCN as outflow indicators is demonstrated in Fig. 18 where we have plotted the FWZI of these lines against the corresponding widths for CO taken from Table 2. Also shown is a comparison between the FWZIs of HCN and HCO⁺ (bottom panel).

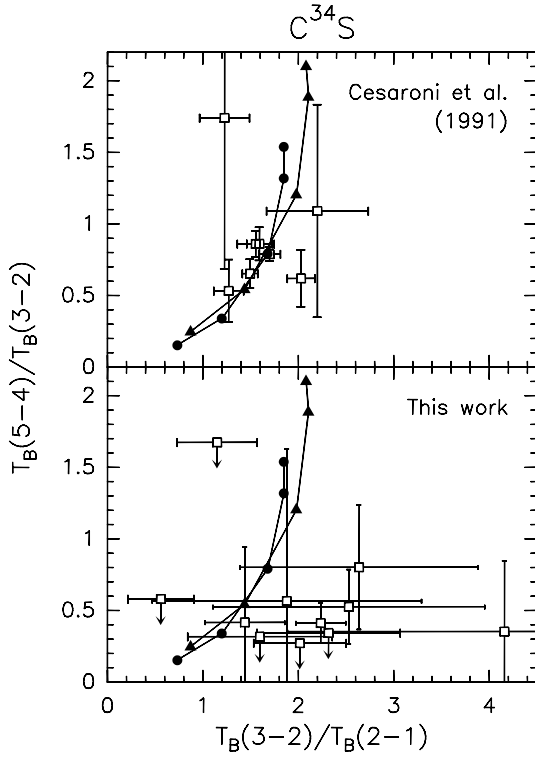


Fig. 10. Plots of the line brightness temperature ratios $T_B(3-2)/T_B(2-1)$ and $T_B(5-4)/T_B(3-2)$ for the $C^{34}S$ lines of the sources in our sample (bottom panel) and in the Cesaroni et al. (1992) study (top panel). The filled points represent the ratios computed with an LVG model for a temperature of 50 K (circles) and 100 K (triangles) and H_2 density of 10^5 , $3 \cdot 10^5$, 10^6 , $3 \cdot 10^6$, and 10^7 cm^{-3} , going from the bottom to the top of the figure

Table 8. Ratios between integrated emission in the main line ($F = 2 - 1$) and in the satellites ($F = 0 - 1$ and $2 - 1$) for the $HCN(1 - 0)$ transition. The LTE values are 0.2 for the $0 - 1/2 - 1$ ratio and 0.6 for $1 - 1/2 - 1$

Name	$0 - 1/2 - 1$	$1 - 1/2 - 1$
NGC 281-W	0.41	0.74
AFGL5142	0.39	0.77
S233	0.43	0.76
GGD 4	0.29	0.50
S235 B	0.35	0.46
MON R2	0.33	0.70
GGD 12-15	0.20	0.41
NGC 2264-C	0.27	0.47
IRAS 20126+4104	0.36	0.67
IC 1396-N	0.79	0.91
L1204-G	0.38	0.42
IRAS 23151+5912	0.30	0.42

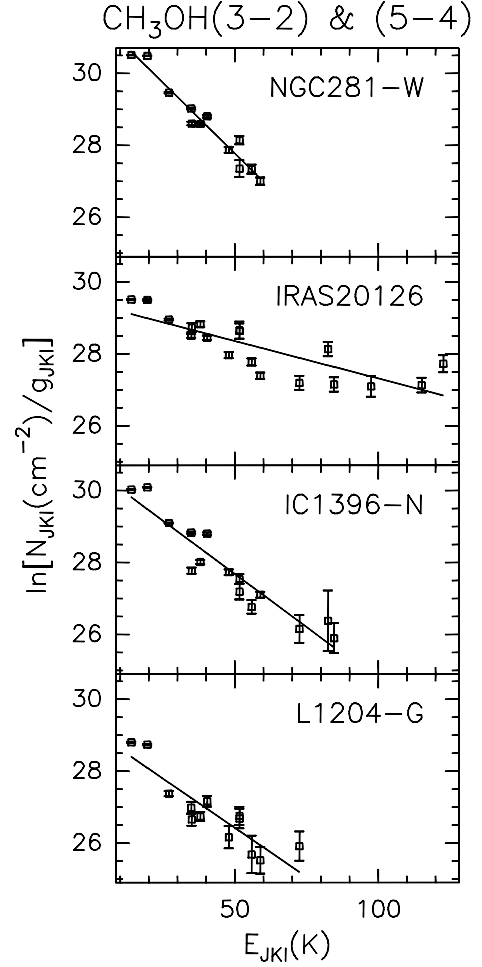


Fig. 11. Boltzmann plots from the $CH_3OH(3-2)$ and $(5-4)$ lines. The column densities are source averaged assuming the deconvolved angular diameters given in Table 11 for CH_3OH . The straight lines represent least square fits to the data. The derived rotation temperatures and column densities are given in Table 12

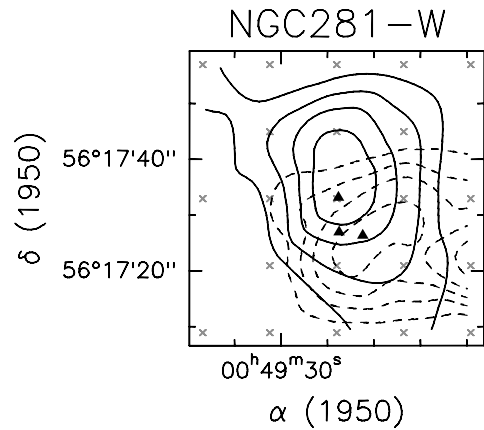


Fig. 12. Map of the $HCO^+(1-0)$ line emission in NGC 281-W integrated from -42 to -36 km s^{-1} (full contours) and from -26 to -20 km s^{-1} (dashed). The contour levels range from 0.7 to 1.9 by 0.3 K km s^{-1} . The triangles indicate the position of the H_2O maser spots

Table 9. a) Results of Gaussian fits to CH₃OH lines towards centre position in NGC 281-W

Line	V_{LSR} (km s ⁻¹)	$FWHM$ (km s ⁻¹)	$\int T_{\text{MB}} dV$ (K km s ⁻¹)
$J = 3 \rightarrow 2$			
1 E1	-30.76 ± 0.07	4.0 ± 0.1	3.1 ± 0.1
2 A ⁺	"	"	1.2 ± 0.1
2 E1 & -2 E2	"	"	3.8 ± 0.1
2 A ⁻	"	"	0.5 ± 0.1
0 A ⁺	-31.12 ± 0.02	5.22 ± 0.03	23.3 ± 0.2
-1 E2	"	"	20.1 ± 0.2
0 E	"	"	8.2 ± 0.2
$J = 5 \rightarrow 4$			
0 E1	-31.5 ± 0.1	4.6 ± 0.2	6.0 ± 0.5
2 E1 & -2 E2	"	"	4.2 ± 0.4
2 A ⁺	"	"	<0.4
1 E1	"	"	3.4 ± 0.4
3 E1	"	"	<0.4
-3 E2	"	"	<0.4
2 A ⁻	"	"	<0.4
3 A ⁻ & A ⁺	"	"	<0.4
4 E1	"	"	<0.4
-1 E2	-31.59 ± 0.09	5.24 ± 0.09	14.6 ± 0.5
-4 E2	"	"	<0.4
4 A ⁻ & A ⁺	"	"	<0.4
0 A ⁺	"	"	19.0 ± 0.5

Table 9. c) Results of Gaussian fits to CH₃OH lines towards centre position in IRAS 20126+4104

Line	V_{LSR} (km s ⁻¹)	$FWHM$ (km s ⁻¹)	$\int T_{\text{MB}} dV$ (K km s ⁻¹)
$J = 3 \rightarrow 2$			
1 E1	-3.7 ± 0.3	8.0 ± 0.2	2.5 ± 0.3
2 A ⁺	"	"	1.4 ± 0.3
2 E1 & -2 E2	"	"	3.4 ± 0.3
2 A ⁻	"	"	1.4 ± 0.3
0 A ⁺	-3.45 ± 0.04	5.43 ± 0.06	6.1 ± 0.1
-1 E2	"	"	5.3 ± 0.1
0 E	"	"	3.5 ± 0.1
$J = 5 \rightarrow 4$			
0 E1	-4.4 ± 0.2	8.0 ± 0.4	5.5 ± 0.5
2 E1 & -2 E2	"	"	5.2 ± 0.5
2 A ⁺	"	"	2.1 ± 0.4
1 E1	"	"	4.4 ± 0.4
3 E1	-4.3 ± 0.5	8.0 ± 0.5	4.2 ± 0.8
-3 E2	"	"	1.5 ± 0.4
2 A ⁻	"	"	<0.2
3 A ⁻ & A ⁺	"	"	3.1 ± 0.6
4 E1	"	"	0.3 ± 0.6
-1 E2	-4.8 ± 0.2	8.6 ± 0.3	8.6 ± 0.5
-4 E2	"	"	1.6 ± 0.4
4 A ⁻ & A ⁺	"	"	1.7 ± 0.4
0 A ⁺	"	"	9.4 ± 0.5

Table 9. b) Results of Gaussian fits to CH₃OH lines towards centre position in IC 1396-N

Line	V_{LSR} (km s ⁻¹)	$FWHM$ (km s ⁻¹)	$\int T_{\text{MB}} dV$ (K km s ⁻¹)
$J = 3 \rightarrow 2$			
1 E1	0.4 ± 0.1	4.5 ± 0.2	1.5 ± 0.1
2 A ⁺	"	"	0.8 ± 0.1
2 E1 & -2 E2	"	"	2.4 ± 0.1
2 A ⁻	"	"	0.5 ± 0.1
0 A ⁺	0.59 ± 0.02	3.83 ± 0.02	16.4 ± 0.1
-1 E2	"	"	15.4 ± 0.1
0 E	"	"	6.4 ± 0.1
$J = 5 \rightarrow 4$			
0 E1	-0.2 ± 0.2	6.9 ± 0.3	5.5 ± 0.4
2 E1 & -2 E2	"	"	5.0 ± 0.4
2 A ⁺	"	"	1.0 ± 0.4
1 E1	"	"	2.0 ± 0.4
3 E1	0.1 ± 0.3	6.2 ± 0.5	0.9 ± 0.8
-3 E2	"	"	<0.3
2 A ⁻	"	"	<0.3
3 A ⁻ & A ⁺	"	"	1.1 ± 0.5
4 E1	"	"	<0.3
-1 E2	0.4 ± 0.1	7.2 ± 0.2	15.5 ± 0.5
-4 E2	"	"	<0.3
4 A ⁻ & A ⁺	"	"	1.2 ± 0.4
0 A ⁺	"	"	16.6 ± 0.5

Table 9. d) Results of Gaussian fits to CH₃OH lines towards centre position in L1204-G

Line	V_{LSR} (km s ⁻¹)	$FWHM$ (km s ⁻¹)	$\int T_{\text{MB}} dV$ (K km s ⁻¹)
$J = 3 \rightarrow 2$			
1 E1	-11.05 ± 0.02	1.68 ± 0.03	0.29 ± 0.05
2 A ⁺	"	"	0.18 ± 0.05
2 E1 & -2 E2	"	"	0.39 ± 0.05
2 A ⁻	"	"	0.20 ± 0.05
0 A ⁺	-11.06 ± 0.01	1.64 ± 0.02	2.76 ± 0.05
-1 E2	"	"	2.30 ± 0.05
0 E	"	"	0.66 ± 0.05
$J = 5 \rightarrow 4$			
0 E1	-11.6 ± 0.4	3.8 ± 0.9	0.9 ± 0.3
2 E1 & -2 E2	"	"	0.8 ± 0.3
2 A ⁺	"	"	0.6 ± 0.2
1 E1	"	"	0.5 ± 0.3
3 E1	"	"	<0.3
-3 E2	"	"	<0.3
2 A ⁻	"	"	<0.3
3 A ⁻ & A ⁺	"	"	<0.3
4 E1	"	"	<0.3
-1 E2	-11.4 ± 0.2	4.1 ± 0.6	2.3 ± 0.3
-4 E2	"	"	<0.3
4 A ⁻ & A ⁺	"	"	<0.3
0 A ⁺	"	"	2.0 ± 0.3

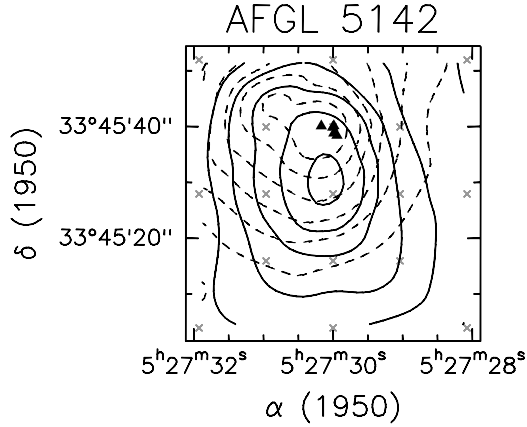


Fig. 13. Map of the CS(3 – 2) line emission in AFGL5142 integrated from -7 to -3 km s^{-1} (full contours) and from -3 to 1 km s^{-1} (dashed). The contour levels range from 7 to 32 by 5 K km s^{-1} . The triangles indicate the position of the H_2O maser spots

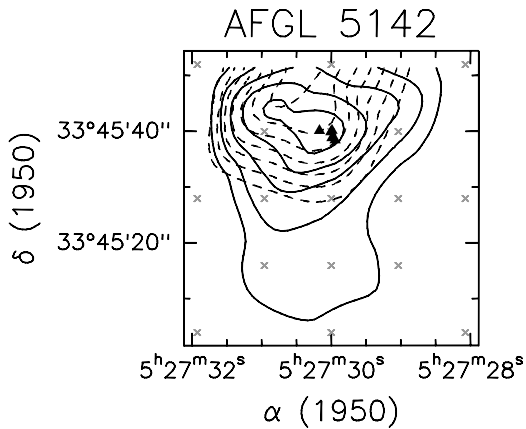


Fig. 14. Map of the $\text{HCO}^+(1-0)$ line emission in AFGL5142 integrated from -19.5 to -7 km s^{-1} (full contours) and from 2.75 to 8.75 km s^{-1} (dashed). The contour levels range from 2 to 15 K km s^{-1} (dashed). The contour levels range from 2 to 5.6 by 0.6 K km s^{-1} . The triangles indicate the position of the H_2O maser spots

One sees that in most sources HCO^+ and HCN , which preferentially sample high density gas, have higher FWZI than CO . One should be clear that this is partially an artifact. The CO data taken from the literature have in general been averaged over larger beams than those ($\sim 25''$) used for HCN and HCO^+ . Thus, they sample gas farther and at lower velocity from the IRAS source. Moreover, the FWZI used in this comparison is a quantity which depends on S/N and hence is not necessarily a good measure of source characteristics. Nevertheless, the line widths measured in HCO^+ , HCN are extremely high and show that a non-negligible fraction of *dense* gas is being accelerated to velocities above 50 km s^{-1} . It is interesting to note also that there is no clear correlation between the FWZI

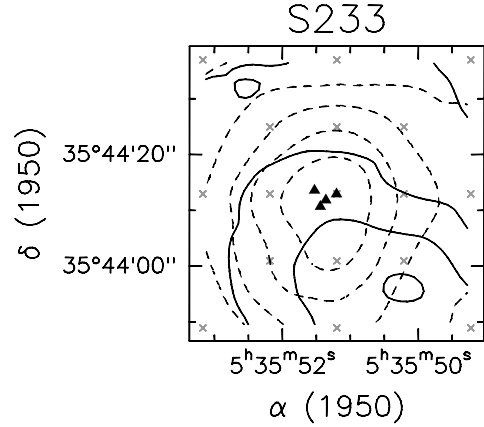


Fig. 15. Map of the CS(3 – 2) line emission in S233 integrated from -20.5 to -17 km s^{-1} (full contours) and from -17 to -13.5 km s^{-1} (dashed). The contour levels range from 5 to 25 by 5 K km s^{-1} . The triangles indicate the position of the H_2O maser spots

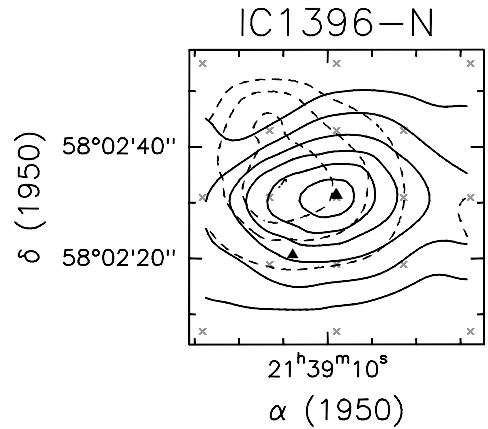


Fig. 16. Map of the CS(3 – 2) line emission in IC 1396-N integrated from -7.25 to -1.25 km s^{-1} (full contours) and from 2.75 to 8.75 km s^{-1} (dashed). The contour levels range from 3 to 13 by 2 K km s^{-1} . The triangles indicate the position of the H_2O maser spots

measured in HCO^+ and HCN , and bolometric luminosity (see second panel of Fig. 18).

We do however find a correlation between the intensity ratio of the $\text{HCN}(1-0)$ and $\text{HCO}^+(1-0)$ lines and the dust temperature as measured by the ratio of 60 μm and 12 μm IRAS fluxes (see Fig. 19 top). We note here that this flux ratio sometimes is found to be less a measure of temperature than a measure of the prevalence of small grains excited by ultra-violet photons and out of thermal equilibrium. We do not know whether that is the case for the sources in our sample. However, we clearly see in Fig. 19 top, tendency for larger $I(\text{HCO}^+)/I(\text{HCN})$ and hence presumably a larger $[\text{HCO}^+]/[\text{HCN}]$ abundance ratio in sources with lower apparent dust

Table 10. Results of Gaussian fits to CH₃CN lines towards centre position in map

$J \rightarrow J-1$	V_{LSR} (km s ⁻¹)	$FWHM$ (km s ⁻¹)	$\int T_{\text{MB}} dV$ (K km s ⁻¹)								
			$K=0$	1	2	3	4	5	6	7	8
NGC 281-W											
8→7	-30.2 ± 0.2	5 ^a	2.4 ± 0.1	2.1 ± 0.1	1.2 ± 0.1	0.2 ± 0.1	<0.3	<0.3	<0.3	<0.3	
12→11	-30.8 ± 0.3	5 ^a	1.4 ± 0.2	1.1 ± 0.2	0.8 ± 0.2	0.9 ± 0.2	<0.8	<0.8	<0.8	<0.8	
AFGL5142											
8→7	-3.1 ± 0.3	5.6 ± 0.5	1.8 ± 0.2	1.5 ± 0.2	1.1 ± 0.1	1.2 ± 0.1	0.4 ± 0.1	<0.3	<0.3	<0.3	
12→11	-3.5 ± 0.2	3.2 ± 0.7	0.3 ± 0.1	0.6 ± 0.1	0.6 ± 0.1	0.8 ± 0.2	<0.6	<0.6	<0.6	<0.6	
S233											
8→7	-16.0 ± 0.3	4 ^a	1.7 ± 0.1	1.4 ± 0.1	0.5 ± 0.1	0.4 ± 0.1	<0.4	<0.4	<0.4	<0.4	
12→11	-16.0 ± 0.3	4 ^a	0.9 ± 0.1	1.1 ± 0.1	<0.9	<0.9	<0.9	<0.9	<0.9	<0.9	
GGD 4											
8→7	1.7 ± 0.3	4 ^a	1.1 ± 0.3	1.1 ± 0.3	<0.4	<0.4	<0.4	<0.4	<0.4	<0.4	
S235 B											
8→7	-17.3 ± 0.4	2 ^a	0.9 ± 0.1	0.6 ± 0.1	<0.5	<0.5	<0.5	<0.5	<0.5	<0.5	
MON R2											
8→7	9.7 ± 0.3	4 ^a	0.7 ± 0.2	0.9 ± 0.2	<0.6	<0.6	<0.6	<0.6	<0.6	<0.6	
NGC 2264-C											
8→7	8.5 ± 0.3	4 ^a	1.0 ± 0.2	0.6 ± 0.2	<0.5	<0.5	<0.5	<0.5	<0.5	<0.5	
IRAS 20126+4104											
8→7	-3.8 ± 0.2	8.3 ± 0.2	3.3 ± 0.2	2.7 ± 0.2	2.6 ± 0.1	2.9 ± 0.1	1.2 ± 0.1	1.1 ± 0.1	1.0 ± 0.1	0.5 ± 0.1	
12→11	-4.3 ± 0.2	7.8 ± 0.2	4.2 ± 0.3	4.6 ± 0.3	4.7 ± 0.3	4.2 ± 0.3	2.6 ± 0.3	2.5 ± 0.2	2.2 ± 0.3	0.7 ± 0.2	0.7 ± 0.2
IC 1396-N											
8→7	-0.6 ± 0.5	5 ^a	0.7 ± 0.1	0.7 ± 0.1	0.7 ± 0.1	0.6 ± 0.1	0.4 ± 0.1	<0.4	<0.4	<0.4	
L1204-G											
8→7	-12.7 ± 1	4 ^a	0.3 ± 0.1	0.5 ± 0.1	<0.4	<0.4	<0.4	<0.4	<0.4	<0.4	

^a Fixed.**Table 11.** Source FWHP and deconvolved angular diameter (in parentheses) in different lines

Source	¹³ CO (arcsec)	HCN (arcsec)	HCO ⁺ (arcsec)	CS (arcsec)	C ³⁴ S(3-2) (arcsec)	CH ₃ OH(3-2) (arcsec)
NGC 281-W	>45 (>44)	46 (37)	45 (36)	29 (25)	24 (17)	28 (22)
AFGL5142	>45 (>44)	>43 (>34)	>38 (>26)	31 (27)	30 (24)	—
S233	>96 (>95)	>46 (>37)	>51 (>43)	≥38 (≥35)	35 (31)	—
GGD 4	37 (35)	45 (36)	—	—	^a	—
S235 B	>96 (>95)	47 (38)	—	—	35 (30)	—
MON R2	>96 (>95)	>96 (>95)	—	—	>38 (>34)	—
GGD 12-15	>96 (>95)	>96 (>95)	—	—	^a	—
NGC 2264-C	>96 (>95)	>96 (>95)	—	—	47 (44)	—
IRAS 20126+4104	>96 (>95)	39 (28)	43 (34)	31 (27)	22 (14)	23 (15)
IC 1396-N	>96 (>95)	49 (41)	>45 (>36)	42 (38)	^a	32 (27)
L1204-G	>96 (>95)	>96 (>95)	>49 (>41)	40 (36)	^a	>22 (>14)
IRAS 23151+5912	32 (30)	37 (26)	46 (37)	24 (18)	27 (21)	—

^a Detected only towards H₂O maser position.

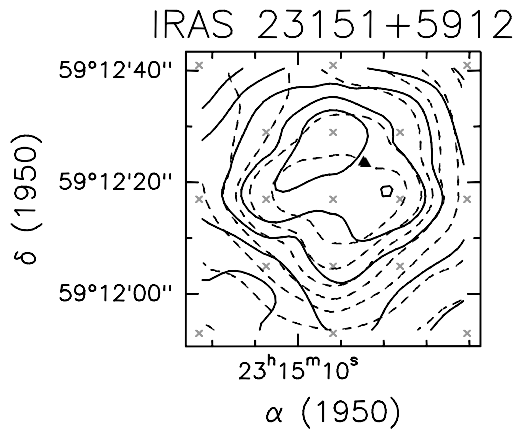


Fig. 17. Map of the $\text{HCO}^+(1-0)$ line emission in IRAS 23151+5912 integrated from -60 to -55 km s^{-1} (full contours) and from -55 to 48 km s^{-1} (dashed). The contour levels range from 0.8 to 4.3 by 0.5 K km s^{-1} . The triangles indicate the position of the H_2O maser spots

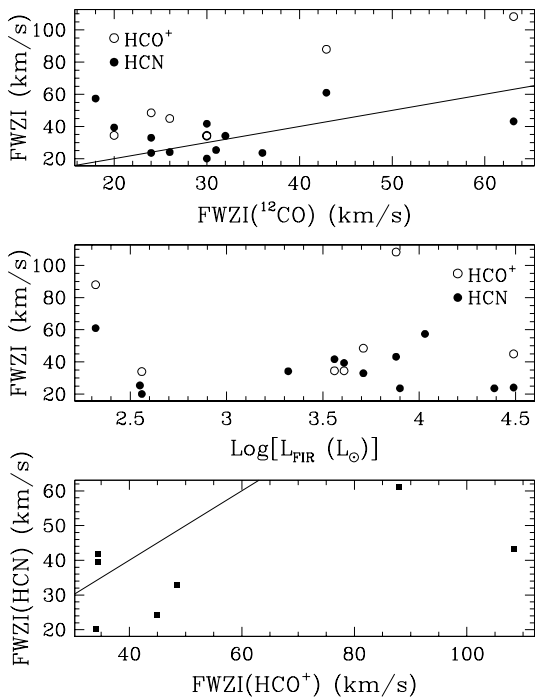


Fig. 18. Top panel: full width at zero intensity of the $\text{HCN}(1-0)$ (filled points) and $\text{HCO}^+(1-0)$ (empty) lines as a function of the FWZI of the $^{12}\text{CO}(1-0)$ line (from Table 2). Middle panel: same as above as a function of the luminosity of the IRAS source. Bottom panel: FWZI of the $\text{HCN}(1-0)$ line versus the FWZI of the $\text{HCO}^+(1-0)$ line

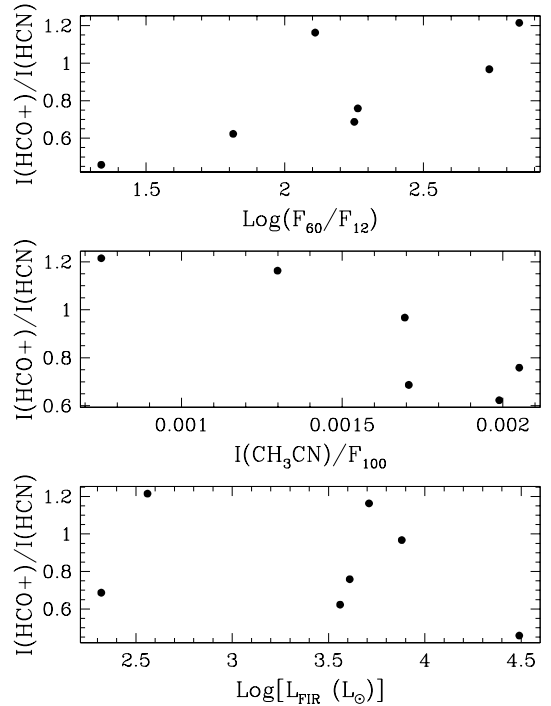


Fig. 19. Ratio of the integrated intensities under the $\text{HCO}^+(1-0)$ and $\text{HCN}(1-0)$ lines as a function of the ratio between the 60 and $12 \mu\text{m}$ IRAS fluxes (top panel), the ratio between the $\text{CH}_3\text{CN}(8-7) K=0+1$ integrated intensity and the $100 \mu\text{m}$ IRAS flux (middle), and the luminosity of the IRAS source (bottom)

temperature (higher $60/12$ flux ratio). The correlation is not of great statistical significance, but seems to us worthy of verification with a larger sample of objects. We note moreover that there is no clear correlation with bolometric luminosity (Fig. 19 bottom) but there is a slight correlation (Fig. 19 middle) when one plots $I(\text{HCO}^+)/I(\text{HCN})$ against $I(\text{CH}_3\text{CN})/F_{100 \mu\text{m}}$. The motivation for considering the latter quantity is that it may be a measure of the relative importance of a possible disk in these sources (assuming that the methyl cyanide emission in some sense measures the disk emission). Here one sees a slight fall-off in the HCO^+ to HCN intensity ratio with increasing relative importance of the methyl cyanide emission. Methyl cyanide seems to appear preferentially in high temperature regions and hence it is possible that Fig. 19 top and middle both are showing a correlation between high dust temperature and high $[\text{HCN}]/[\text{HCO}^+]$ abundance ratio (or alternatively between the fraction of “very small grains” and the $[\text{HCN}]/[\text{HCO}^+]$ abundance ratio).

7. Conclusions

We performed a survey in up to seven molecular transitions towards a sample of twelve water masers with luminous IRAS counterparts. All sources but one (AFGL5142)

Table 12. Rotation temperatures and column densities derived from the rotational diagrams of CH₃OH (see Fig. 11)

Source	T_{rot} (K)	$N_{\text{CH}_3\text{OH}}^a$ (10^{15} cm^{-2})
NGC 281-W	13	1.7
IRAS 20126+4104	48	1.2
IC 1396-N	17	0.90
L1204-G	18	0.23

^a Source averaged, assuming the deconvolved CH₃OH angular diameters given in Table 11.

were not found to be positionally associated with 3.6 cm continuum emission in the VLA survey of TFTH: this should bias the sample towards embedded high-mass (proto)stars which are too young to develop an UC HII region. Both high and low density tracers have been observed. In all cases, a compact molecular clump is detected at the position of the H₂O masers, suggesting that we are looking at the envelopes around young deeply embedded massive stars. Such an idea is confirmed by the broad and – in a few transitions – complex line profiles, which indicate significant turbulence and large velocity fields in the regions. The picture is further supported by the existence of outflows in some sources, arising from embedded young stellar objects. Given the high luminosity and the association with H₂O masers, and the embedded nature of the YSOs, we believe that our sample represents an excellent target for future detailed studies of high-mass star formation.

Acknowledgements. This project was partially supported by ASI grants ARS-96-66 and ARS-98-116 to the Osservatorio Astrofisico di Arcetri.

References

- Bachiller R., Codella C., Colomer F., Liechti S., Walmsley C.M., 1998, A&A 335, 266
- Brand J., Cesaroni C., Caselli, et al., 1993, A&AS 103, 541
- Cesaroni R., Walmsley C.M., Kömpe C., Churchwell E., 1991, A&A 252, 278
- Cesaroni R., Churchwell E., Hofner P., Walmsley C.M., Kurtz S., 1994, A&A 288, 903
- Cesaroni R., Felli M., Testi L., Walmsley C.M., Olmi L., 1997a, A&A 325, 725
- Cesaroni R., Hofner P., Walmsley C.M., Churchwell E., 1997b, A&A 331, 709
- Churchwell E., Felli M., Wood D.O.S, Massi M., 1987, ApJ 321, 516
- Churchwell E., Walmsley C.M., Cesaroni R., 1990, A&AS 83, 119
- Codella C., Testi L., Cesaroni R., 1997, A&A 325, 282
- Comoretto G., Palagi F., Cesaroni R., et al., 1990, A&AS 84, 179
- Elitzur M., Hollenbach D.J., McKee C.F., 1989, ApJ 346, 983
- Felli M., Churchwell E., Wilson T.L., Taylor G.B., 1993, A&AS 98, 137
- Felli M., Testi L., Valdetaro R., Wang J.-J., 1997, A&A 320, 594
- Fukui Y., Iwata T., Mizuno A., Bally J., Lane A.P., 1993, E.H. Levy, J.I. Lunine (eds.) Molecular Outflows, in: Protostars and Planets III. The Univ. of Arizona Press, Tucson, p. 603
- Gaume R.A., Wilson T.L., Vrba F.J., Johnston K.J., Schmid-Burgk J., 1998, ApJ 493, 940
- Henning Th., Martin K., Reimann H.-G., et al., 1994, A&A 288, 282
- Hodapp K.-W., 1994, ApJS 94, 615
- Hofner P., Churchwell E., 1996, A&AS 120, 283
- Hunter T.R., Taylor G., Felli M., Tofani G., 1994, A&A 284, 215
- Hunter T.R., Testi L., Taylor G., et al., 1995, A&A 302, 249
- Johnston K.J., Gaume R., Stolovy S., et al., 1992, ApJ 385, 232
- Krügel E., Güsten R., Schulz A., Thum C., 1987, A&A 185, 283
- Margulis M., Lada C.J., Snell R.L., 1988, ApJ 333, 316
- Megeath S.T., Wilson T.L., 1997, AJ 114, 1106
- Millar T.J., 1997, Models of Hot Molecular Cores, in: van Dishoeck E.F. (ed.) Proc. IAU Symp. 178, Molecules in Astrophysics: Probes and Processes. Kluwer, Dordrecht, p. 75
- Menten K.M., Walmsley C.M., Henkel C., Wilson T.L., 1986, A&A 157, 318
- Nakano M., Yoshida S., 1986, PASJ 38, 531
- Ohishi M., 1997, Observations of “Hot Cores”, in: van Dishoeck E.F. (ed.) Proc. IAU Symp. 178, Molecules in Astrophysics: Probes and Processes. Kluwer, Dordrecht, p. 61
- Olmi L., Cesaroni R., Walmsley C.M., 1993, A&A 276, 489
- Olmi L., Cesaroni R., Walmsley C.M., 1996a, A&A 307, 599
- Olmi L., Cesaroni R., Neri R., Walmsley C.M., 1996b, A&A 315, 565
- Palagi F., Cesaroni R., Comoretto G., Felli M., Natale V., 1993, A&AS 101, 153
- Plume R., Jaffe D.T., Evans II N.J., 1992, ApJS 78, 505
- Plume R., Jaffe D.T., Evans II N.J. Martin-Pintado J., Gómez-González J., 1997, ApJ 476, 730
- Rudolph A., Welch W.J., Palmer P., Dubrulle B., 1990, ApJ 363, 528
- Schreyer K., Helmich F.P., van Dishoeck E.F., Henning Th., 1997, A&A 326, 347
- Serabyn E., Güsten R., Mundy L., 1993, ApJ 404, 247
- Snell R.L., Dickman R.L., Huang Y.-L., 1990, ApJ 352, 139
- Testi L., Felli M., Persi P., Roth M., 1994, A&A 288, 634
- Testi L., Felli M., Persi P., Roth M., 1998, A&A 129, 495
- Testi L., Felli M., Persi P., 1999 (in preparation)
- Tofani G., Felli M., Taylor G.B., Hunter T.R., 1995, A&AS 112, 299 (TFTH)
- Turner J.L., Welch W.J., 1984, ApJ 287, L81
- Turner B.E., Chan K.-W., Green S., Lubowich D.A., 1992, ApJ 399, 114

- Walmsley C.M., 1987, *Molecular Clouds Temperature and Density Determinations and What They Teach Us*, in: Morfill G.E., Scholer M. (eds.) NATO/ASI Series Vol. 210, *Physical Processes in Interstellar Clouds*. Reidel, Dordrecht, p. 161
- Welch W.J., Drehrer J.W., Jackson J.M., Tereby S., Vogel S.N., 1987, *Sci* 238, 1550
- Wilson T.L., Rood R.T., 1994, *ARA&A* 32, 191
- Wink J.E., Duvert G., Guilloteau S., et al., 1994, *A&A* 281, 505
- Wood D.O.S., Churchwell E., 1989a, *ApJS* 69, 831
- Wood D.O.S., Churchwell E., 1989b, *ApJ* 340, 265
- Wyrowski F., Hofner P., Schilke P., et al., 1997, *A&A* 320, L17